Geophysical Prospecting

EAGE EUROPEAN ASSOCIATION OF GEOSCIENTISTS & ENGINEERS

Geophysical Prospecting, 2016 doi: 10.1111/1365-2478.12403

Static and dynamic pressure sensitivity anisotropy of a calcareous shale

Oliver N. Ong[1], Douglas R. Schmitt[1]*, Randolph S. Kofman[1] and Kristine Haug[2]

[1] *Institute for Geophysical Research, Department of Physics, 4-138 CCIS, University of Alberta, Edmonton, AB T6G 2E1, Canada, and* [2] *Alberta Energy Regulator, Alberta Geological Survey, Edmonton, AB T6B 2X3, Canada*

Received November 2015, revision accepted March 2016

ABSTRACT

Optimizing the productivity of nonconventional, low-permeability "shale" reservoirs requires detailed knowledge of the mechanical properties of such materials. These rocks' elastic anisotropy is acknowledged but usually ignored due to difficulties in obtaining such information. Here we study in detail the dynamic and static elastic properties of a suite of calcareous mudstones from the nonconventional Duvernay reservoir of Alberta, Canada. The complete set of transversely isotropic elastic constants is obtained from strategically oriented ultrasonic transducers to confining pressures of 90 MPa. Wave speed anisotropies of up to 35% are observed at even the highest confining pressures. Furthermore, the stress sensitivity of the wave speeds, and hence moduli, is itself highly dependent on direction with speeds taken perpendicular to the bedding plane being highly nonlinearly dependent on pressure, whereas those along the bedding plane show, unexpectedly, nearly no pressure dependence. These observations are in qualitative agreement with the preferentially oriented porosity and minerals seen in scanning electron microscope images. These results may be significant to the interpretation of sonic logs and azimuthal amplitude versus offset for principal stress directions, for the concentration of stress within such formations, and for estimation of static engineering moduli from sonic log wave speeds.

Key words: Acoustics, Anisotropy, Petrophysics, Rock Physics, Seismics.

INTRODUCTION

Numerous workers have commented that sedimentary basins are predominantly filled with rocks that are generically called "shales", that such rocks are expected to be elastically anisotropic, and that ignoring this anisotropy affects the quality of seismic images even in regions with flat-lying stratigraphy. This last aspect, reinforced by Thomsen (1986), motivated many theoretical, experimental, and modelling efforts to better understand shale seismic anisotropy over the last 30 years. To some degree, assimilation of these findings into general practice has been slow even though the utility of incorporating anisotropy has been recognized.

However, at this writing, the growth of hydrocarbon production from these "shales" formerly at best considered as source and seal rock has revolutionized the petroleum industry in North America. Direct recovery of high-quality oil and natural gas that are made accessible by hydraulic stimulations has opened up new reserves that were not previously accounted. Such production demands that we have improved knowledge of the anisotropic physical properties of these rocks as this information is, in addition to the more traditional needs of reflection seismic imaging, necessary to comprehending *in situ* states of stress (e.g., Gholami *et al.* (2015) and Amadei (1996)) and the initiation and growth of hydraulic fractures (e.g., Aghighi and Rahman (2010); Vahid and Ahmad (2011); and Waters, Lewis, and Bentley (2011)); to predicting the stability of boreholes drilled through such formations (e.g., Jin *et al.* (2012); Jia *et al.* (2014); Ong and Roegiers (1996); Gaede *et al.* (2012); and Holt *et al.* (2015b); to improving the location of micro-seismic events (e.g., King and Talebi (2007) and Li *et al.* (2014)) and the interpretation of their focal

*E-mail: dschmitt@ualberta.ca

mechanisms (e.g., Vavryčuk (2005) and Kawasaki and Tanimoto (1981)); and to evaluating seismic hazard (Maxwell, Zhang, and Damjanac 2014). Properly addressing these issues also often requires that we have knowledge of the "static" properties that usually differ from the corresponding dynamic moduli that are determined from wave propagation.

Aside from notable exceptions (Kaarsberg 1959), there were few direct laboratory measurements of the anisotropic properties of "shales" probably because they are difficult to work with and characterize and they were not considered reservoir rock. It is usually presumed that such rocks have transversely isotropic (i.e., hexagonal) symmetry and as such must be described by five independent elastic parameters. Thomsen (1986) was able to collect from the open literature and internally reports 17 examples only with a complete set of transversely isotropic elastic constants, a number that had rapidly increased substantially in the compilation of Cholach and Schmitt (2006) that incorporated comprehensive measurement campaigns by Wang (2002b), Vernik and Liu (1997), and Johnston and Christensen (1995). The number of experimental studies has dramatically grown since that time, and the bulk of these studies measure P- and S-wave speeds through core plugs with axes cut at a minimum of three strategic orientations with respect to the shale symmetry by placement of ultrasonic transducers around a single cylindrical sample (Dewhurst and Siggins 2006; Wang 2002a; Sarout and Gueguen 2008a; Sarout *et al.* 2014; Jakobsen and Johansen 2000; Holt *et al.* 2015a; Holt *et al.* 2012), at the ends of at least three cored cylinders or on the flat faces of specially machined polyhedra (Wong *et al.* 2008; Cheadle, Brown, and Lawton 1991; Homand *et al.* 1993; Melendez Martinez and Schmitt 2015). With regard to multi-faced polyhedral, the measurements of Nara *et al.* (2011) with a 98-faced sample and of Lokajicek and Svitek (2015) on spherical samples allowing 132 different directions to be sampled are worth noting although these authors have not studied sedimentary rocks. The same spherical apparatus was used by Nadri *et al.* (2012) on a shale sample from NW Australia. Recent developments that employ laser interferometry show promise (Blum, Adam, and van Wijk 2013) for increasing the number of directions sampled. These last methods are important as sufficient information is collected that no *a priori* assumptions need be made with regard to the material symmetry. Other recent contributions that made measurement on plugs taken only parallel and perpendicular to the bedding planes cannot, without assumptions, completely describe the presumed transverse isotropy but still provide useful information (e.g., Miller, Plumb, and Boitnott (2013) and Sone and Zoback (2013)).

Under pseudo-static loading conditions, there are numerous studies that examine the anisotropic rock strengths (e.g., Heng *et al.* (2015) and McLamore and Gray (1967)), but usually, the strains are not analysed to provide elastic moduli. Exceptions to this include Chenevert and Gatlin (1965) who clearly demonstrated the anisotropy by measuring the strains induced by uniaxially loading cylinders and rectangular prisms of two shales and Niandou *et al.* (1997) who determined from three appropriately oriented samples the complete set of Poisson's ratios and Young's moduli of Tournemire shales during uniaxial loading. Gautam and Wong (2006) use a combination of uniaxial compression and torsion measurements on vertically and horizontally oriented cores of a Colorado shale. Most recently, Islam and Skalle (2013) have demonstrated the anisotropy of a compressible Pierre shale but were not able to obtain a full set of elastic constants.

In this study, we focus on stiff calcareous shales of the Duvernay Formation, Alberta, Canada. The "Duvernay" holds particularly large resource estimated to hold upwards of 44.1 bbl–82.9 bbl of oil, 7.5 bbl–16.3 bbl of natural gas liquids, and 353 Tcf–540 Tcf of natural gas (Rokosh *et al.* 2012). Even a small improvement in recovery rates translates to a large bulk economic gain. More urgently, however, this shale formation is garnering a great deal of interest because of the possible linkage between hydraulic fracture stimulations within the Duvernay, and felt-induced seismicity as large as $4.3M_w$ (AGS 2015) and understanding this material's mechanical properties are also of interest. In this contribution, we describe a series of measurements of the static and dynamic elastic properties on Duvernay Formation cores. We find that not only the Duvernay shale is highly anisotropic but also that the sensitivity of the elastic moduli to stress strongly varies with direction. We organize this paper into sections that briefly review the essential equations of anisotropic elasticity, characterize the materials, describe the experiments that show these rocks to be highly anisotropic, and discuss the implications for comparison between static and dynamic moduli.

BACKGROUND

Forms of Hooke's law

There are now many discussions of anisotropic elasticity in the literature, and we direct the reader to any of the many contributions available for overviews of general elasticity, including the definitions of stress and strain, the statement of Hooke's

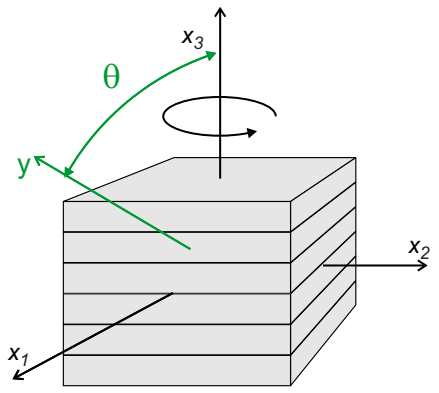

Figure 1 Reference Cartesian x_1–x_2–x_3 coordinate system with the rotational axis of symmetry parallel to x_3 from which angle θ is measured. The x_1–x_2 plane is the bedding or isotropic plane.

law (e.g., Jaeger, Cook, and Zimmerman (2007)), or the solution of Christoffel's equation in determining the phase speeds and polarizations of the three plane waves that will generally propagate in any direction through an anisotropic medium (e.g., Auld (1973)). We presume here that the shales studied are transversely isotropic with the rotational axis of symmetry parallel to the x_3-axis with the material's isotropic "bedding" and x_1–x_2 coordinate system planes identical (Fig. 1). In this situation, the material is described by five independent elastic parameters that, depending on the situation, will be either the stiffness values C_{11}, C_{33}, C_{44}, C_{66}, and C_{13} or the compliance values S_{11}, S_{33}, S_{44}, S_{66}, and S_{13} that in Voigt's (1928) vector and matrix notation allow the generalized Hooke's law relating stress $\boldsymbol{\sigma} = [\sigma_{11}\ \sigma_{22}\ \sigma_{33}\ \sigma_{23}\ \sigma_{13}\ \sigma_{12}] \equiv [\sigma_1\ \sigma_2\ \sigma_3\ \sigma_4\ \sigma_5\ \sigma_6]$ to strain $\boldsymbol{\varepsilon} = [\varepsilon_{11}\ \varepsilon_{22}\ \varepsilon_{33}\ \varepsilon_{23}\ \varepsilon_{13}\ \varepsilon_{12}] \equiv [\varepsilon_1\ \varepsilon_2\ \varepsilon_3\ \varepsilon_4\ \varepsilon_5\ \varepsilon_6]$

$$\boldsymbol{\sigma} = \begin{bmatrix} \sigma_1 \\ \sigma_2 \\ \sigma_3 \\ \sigma_4 \\ \sigma_5 \\ \sigma_6 \end{bmatrix} = \begin{bmatrix} C_{11} & C_{11}-2C_{66} & C_{13} & 0 & 0 & 0 \\ C_{11}-2C_{66} & C_{11} & C_{13} & 0 & 0 & 0 \\ C_{13} & C_{13} & C_{33} & 0 & 0 & 0 \\ 0 & 0 & 0 & C_{44} & 0 & 0 \\ 0 & 0 & 0 & 0 & C_{44} & 0 \\ 0 & 0 & 0 & 0 & 0 & C_{66} \end{bmatrix} \begin{bmatrix} \varepsilon_1 \\ \varepsilon_2 \\ \varepsilon_3 \\ 2\varepsilon_4 \\ 2\varepsilon_5 \\ 2\varepsilon_6 \end{bmatrix} = \boldsymbol{C\varepsilon}, \quad (1)$$

or

$$\epsilon = \begin{bmatrix} \epsilon_1 \\ \epsilon_2 \\ \epsilon_3 \\ 2\epsilon_4 \\ 2\epsilon_5 \\ 2\epsilon_6 \end{bmatrix} = \begin{bmatrix} S_{11} & S_{11}-S_{66}/2 & S_{13} & 0 & 0 & 0 \\ S_{11}-S_{66}/2 & S_{11} & S_{13} & 0 & 0 & 0 \\ S_{13} & S_{13} & S_{33} & 0 & 0 & 0 \\ 0 & 0 & 0 & S_{44} & 0 & 0 \\ 0 & 0 & 0 & 0 & S_{44} & 0 \\ 0 & 0 & 0 & 0 & 0 & S_{66} \end{bmatrix} \begin{bmatrix} \sigma_1 \\ \sigma_2 \\ \sigma_3 \\ \sigma_4 \\ \sigma_5 \\ \sigma_6 \end{bmatrix} = S\sigma, \quad (2)$$

with

$$S = C^{-1}. \quad (3)$$

Sayers (2013), among others, provides more direct relations between C_{ij} and S_{ij}.

The stiffnesses of equation (1) are preferred when working with dynamic wave propagation and are most often seen by geophysicists. In contrast, the compliances of equation (2) are more conveniently obtained by measuring strains induced by applied stresses, and as such, the compliance matrix S in terms of engineering moduli

$$S = \begin{bmatrix} 1/E_1 & -\nu_{21}/E_1 & -\nu_{31}/E_3 & 0 & 0 & 0 \\ -\nu_{12}/E_1 & 1/E_1 & -\nu_{31}/E_3 & 0 & 0 & 0 \\ -\nu_{13}/E_1 & -\nu_{13}/E_1 & 1/E_3 & 0 & 0 & 0 \\ 0 & 0 & 0 & 1/\mu_{31} & 0 & 0 \\ 0 & 0 & 0 & 0 & 1/\mu_{13} & 0 \\ 0 & 0 & 0 & 0 & 0 & 1/\mu_{12} \end{bmatrix}, \quad (4)$$

with the various Young's E_i and shear μ_{ij} moduli and the Poisson's ratios ν_{ij} described in Fig. 2. Examination of equation (4) in light of the symmetry of S together with the requirement that there be at most five independent moduli demands $\nu_{21} = \nu_{12}$, $\nu_{13}/\nu_{31} = E_1/E_3$, and $\mu_{13} = \mu_{31}$. Melendez Martinez and Schmitt (2015) review a number of the relationships between equations (1), (2), and (4) useful for converting between stiffnesses, compliances, and engineering moduli; we include these in Appendix A for the sake of completeness.

In this study, we obtain a full set of dynamic elastic stiffnesses by measuring the wave speeds in a number of strategic directions with respect to the material's axis of symmetry, as shown in Fig. 3; the linkages between the six observed speeds and the five stiffness values required to define the transversely

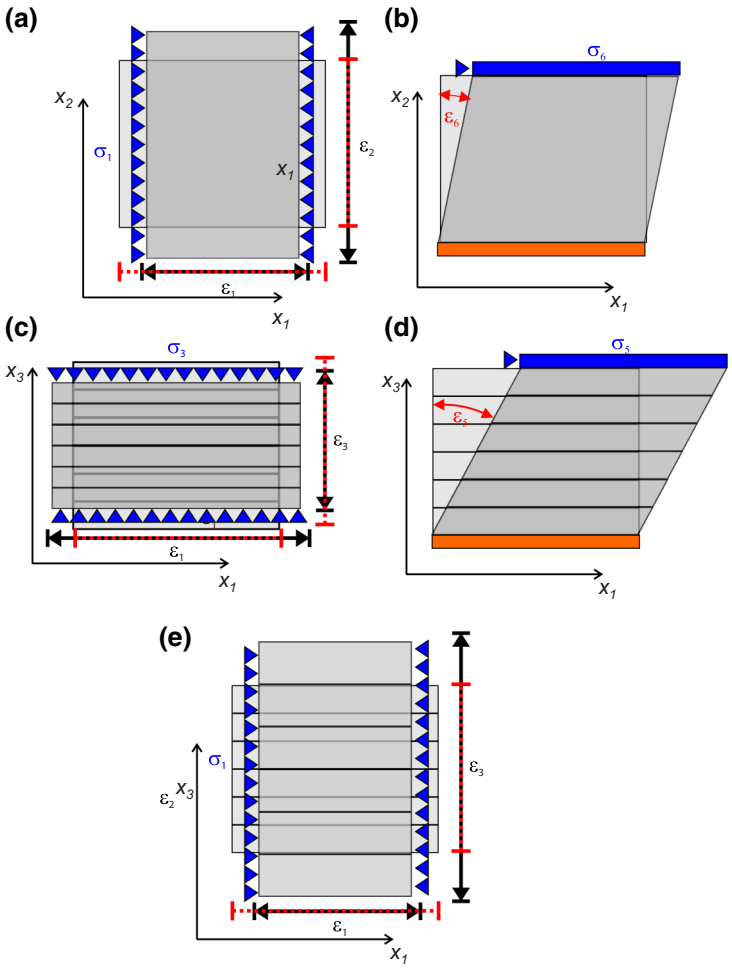

Figure 2 Illustration of the deformations associated with the definitions of the engineering moduli of the transversely isotropic block in Fig. 1. Applied stresses represented as blue arrowheads applied to the surface of the material. Orange edges represent surfaces that cannot be moved during the experiment. Original and final shapes represented by light and dark grey zones, respectively, and the changes in the lengths of appropriately oriented fibres in the material are the differences between the red dashed lines and the black arrows that would define the strains. Moduli in the isotropic x_1–x_2 plane with (a) $E_1 = -\sigma_1/\varepsilon_1$ and $\nu_{12} = -\varepsilon_2/\varepsilon_1$ from application of a uniaxial compression $\boldsymbol{\sigma}_1$ and (b) $\mu_{12} = \boldsymbol{\sigma}_6/\varepsilon_6$ from application of shear stress $\boldsymbol{\sigma}_6$. Moduli associated with the vertical plane include (c) $E_3 = -\boldsymbol{\sigma}_3/\varepsilon_3$ and $\nu_{31} = -\varepsilon_1/\varepsilon_3$ from application of uniaxial compression $\boldsymbol{\sigma}_3$, (d) $\mu_{13} = \boldsymbol{\sigma}_5/\varepsilon_5$ from the application of shear stress $\boldsymbol{\sigma}_5$, and (e) $\nu_{13} = -\varepsilon_3/\varepsilon_1$ obtained during the same application of $\boldsymbol{\sigma}_1$ as in panel (a).

isotropic material have been described many times in the literature (e.g., Auld (1973) and Sarout *et al.* (2007)), and we provide only the final relationships that are used later to calculate the stiffness values:

$$\mathbf{C}_{11} = \rho V_P{}^2(90^\circ). \tag{5}$$

$$\mathbf{C}_{33} = \rho V_P{}^2(0^\circ). \tag{6}$$

$$\mathbf{C}_{44} = \rho V_{SH}{}^2(0^\circ). \tag{7}$$

$$\mathbf{C}_{66} = \rho V_{SH}{}^2(90^\circ). \tag{8}$$

$$\mathbf{C}_{13} = -\mathbf{C}_{44} + \frac{1}{2}\Big[\left(4\rho V_P{}^2(45^\circ) - \mathbf{C}_{11} - \mathbf{C}_{33} - 2\mathbf{C}_{44}\right)^2 - (\mathbf{C}_{11} - \mathbf{C}_{33})^2\Big]^{\frac{1}{2}}. \tag{9}$$

In the above equations, subscripts *P*, *SV*, and *SH* indicate the polarization of the wave to be longitudinal, transverse within any plane containing the X_3-axis, and transverse within the X_1–X_2 plane. The propagation direction is denoted by the angle *q*, as indicated in Fig. 1. Examination of equations (5)–(9) shows that these elastic constants can be determined with relative ease and accuracy through measurements of wave speeds along the principal axes of the medium. Estimation of $\mathbf{C}_{13}$, however, is not as straightforward due to the complexity of the equation yielding large uncertainties through the propagation of errors.

Alternative expressions for $\mathbf{C}_{13}$ can be derived, which include the 45° quasi-shear velocity in addition to the quasi-compressional (Hemsing 2007)

$$\mathbf{C}_{13} = -\mathbf{C}_{44} + \frac{1}{2}\sqrt{4\rho^2\left(\left(V_P{}^2(45^\circ) - V_{SV}{}^2(45^\circ)\right)^2 - (\mathbf{C}_{11} - \mathbf{C}_{33})^2}, \tag{10}$$

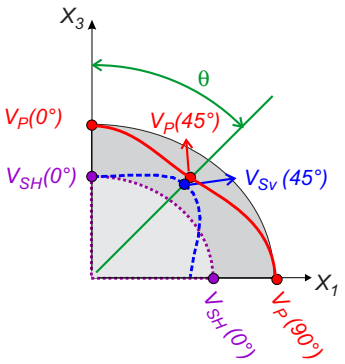

Figure 3 View of hypothetical wave speed surfaces for the longitudinal polarization *P* in red, the horizontal polarization *SH* (i.e., parallel to the x_1–x_2 plane) in purple, and the vertical polarization *SV* (i.e., parallel to the x_1–x_3 plane) in blue. The coloured dots represent the six wave speeds measured here in directions along the vertical ($\theta = 0°$), the horizontal ($\theta = 90°$), and obliquely ($\theta = 45°$). The light-filled ellipse represents the elliptical *SH* wave surface, and the dark-filled ellipse represents the special case of elliptical anisotropy for the P-wave surface when Thomsen's (1986) $\delta = \varepsilon$.

or use ${V_{SV}}^2(45^\circ)$ exclusively in the cases where (${V_P}^2(45^\circ)$ may be unavailable

$$C_{13} = -C_{44} + \frac{1}{2}\sqrt{\left(C_{11} + C_{33} + 2C_{44} - 4\rho {V_{SV}}^2(45^\circ)\right)^2 - \left(C_{11} - C_{33}\right)^2}. \quad (11)$$

as will be necessary later in one of our analyses due to transducer failure.

Elastic moduli can be either estimated from directly measuring the deformation (static) or calculated using the phase velocities and bulk density of the material (dynamic). Historically, studies have shown discrepancies between static and dynamic moduli in materials of TI symmetry (e.g., Hofman (2006); King (1969); Sone and Zoback (2013); Cheng and Johnston (1981); and Mashinsky (2003)) with the dynamic moduli almost always exceeding the static significantly although this may not always be the case (Ciccotti and Mulargia 2004). This difference is problematic in that it is not clear how one should employ seismic or sonic log observations to supply quantitative moduli for engineering deformation calculations. Here we compare simultaneous strain (static) to ultrasonic (dynamic) moduli under a hydrostatic confining pressure.

The linear compressibility λ_i (Brace 1965) or, conversely, the linear stiffness Kl_i (Ruiz Pena 1998; Meléndez Martinez 2014) describes the relationship between the linear strains $\boldsymbol{\varepsilon}_i$ induced parallel to direction i subject to a change in the hydrostatic stress dp

$$\lambda_i = \frac{1}{Kl_i} = -\frac{d\boldsymbol{\varepsilon}_i}{dp}. \quad (12)$$

It is much easier to apply a hydrostatic pressure to a rock sample than a full triaxial state of stress, and because of this, many of the earliest rock elasticity and, indeed, anisotropy measurements are used λ_i (e.g., Zisman (1933)). Of course, no information on the static shear moduli can be obtained by measuring strains under hydrostatic compression.

The measurements in this study are made under hydrostatic stresses, and we take advantage of this by measuring, using strain gauges, the strains $\boldsymbol{\varepsilon}_1$ and $\boldsymbol{\varepsilon}_3$ perpendicular, to the isotropic bedding plane of the sample. These strain results are quasi-statically measured and can be compared with the stiffnesses obtained from the ultrasonic wave speeds via (Melendez Martinez and Schmitt 2015)

$$Kl_1 = Kl_2 = \frac{2\mathbf{C}_{33}(\mathbf{C}_{11} - \mathbf{C}_{66}) - 2{\mathbf{C}_{13}}^2}{\mathbf{C}_{33} - \mathbf{C}_{13}}. \quad (13)$$

and

$$Kl_3 = \frac{\mathbf{C}_{33}(\mathbf{C}_{11} - \mathbf{C}_{66}) - {\mathbf{C}_{13}}^2}{\mathbf{C}_{11} - \mathbf{C}_{66} - \mathbf{C}_{13}}. \quad (14)$$

Equations (13) and (14) provide a means to directly compare the dynamic ultrasonic to the static strain measurements.

SAMPLE CHARACTERIZATION

The Duvernay Formation samples are from depths between 2871.60 m and 2882.96 m in borehole *02-17-043-04 W5* in the Alberta Township System coordinate system (52.670°N, 114.470°W). The Duvernay Formation is a depositional unit within the upper Devonian Woodbend Group and is considered to be the source rock for many conventional hydrocarbon accumulations such as the prolific Leduc, Nisku, and Swan Hills reservoirs. The deposition of the Duvernay Formation is characterized by extensive basin deposits resulting from transgression of the Devonian sea and is laterally equivalent to the Leduc reefs. The formation is divided between the East and West Shale Basins where it is overlain by the Ireton Formation and overlies the upper Majeau Lake Formation except in the southern end where it overlies the Cooking Lake Formation.

The East Shale Basin lithology is dominated by organic-rich lime mudstone and grades laterally into shallow-water carbonate equivalents of the Grosmont shelf complex. In the West Shale Basin, the Duvernay Formation thins away from the reef complexes and is dominated by characteristic

radioactive shales seen in the natural gamma ray logs (Fig. 4). As a whole, the formation tends to thicken from east to west with the same trend in thermal maturity covering a range from immature in the east to overmature in the west. Total organic carbon (TOC) ranges of 0.1 wt.%–11.1 wt.% have been reported based on samples obtained from 50 wells and found that samples from the East Shale Basin contained the greatest amount of TOC. Overall, the formation is estimated to host approximately 443 Tcf of natural gas and 61.7 bbl of oil (Rokosh *et al.* 2012).

The four calcareous mudstone samples used in this study were taken from the same well at similar but different depths. X-ray powder diffraction analysis was conducted using a Rigaku Ultima IV diffractometer to qualitatively identify the major constituent minerals. TOC is determined through a dry combustion method using a Shimadzu TOC-V CHS/CSN analyser where any inorganic carbon is first removed by acidifying the sample with a 6% HCl solution. These characteristics are displayed in Table 1. As all samples are from the same well and at similar depths, TOC values are expectedly very similar as well, with samples 7–13 having a slightly lower value. Mineral modes were not determined, but a typical Duvernay sample (Anderson *et al.* 2010) would principally consist of ~30% quartz and feldspar, ~50% carbonates, and 20% phyllites (primarily muscovite and illite). There were no detectable montmorillonite series clays in these samples.

Petrophysical properties (Table 2) of the samples were determined through mercury intrusion Porosimetry using a Micromeritics AutoPore IV capable of resolving pores of diameters between 360 μm and 0.003 μm. The porosities so determined are relatively low falling in the range from 2.5% to 3.8%.

The microscopic structure and porosity of such rocks has received a great deal of attention recently with a number of workers using a wide variety of techniques (Anderson *et al.* 2010; Wüst, Nassichuk, and Bustin 2013; Clarkson *et al.* 2013; Sondergeld *et al.* 2010), including scanning electron microscopy (SEM). SEM images were also acquired here from sample 5-13 but more with a view to studying the rocks fabric, and as such, images were made at different orientations. Bedding planes are readily apparent at low magnification (Fig. 5a), whereas the preferential orientations of illite subparallel to the bedding are seen at greater magnification (Fig. 5b). This orientation persists when seen from a direction perpendicular the bedding plane where the material appears as sheet-like surfaces (Fig. 5c). These images appear to suggest that both bedding layers and mineralogic orientations influence the material's anisotropy.

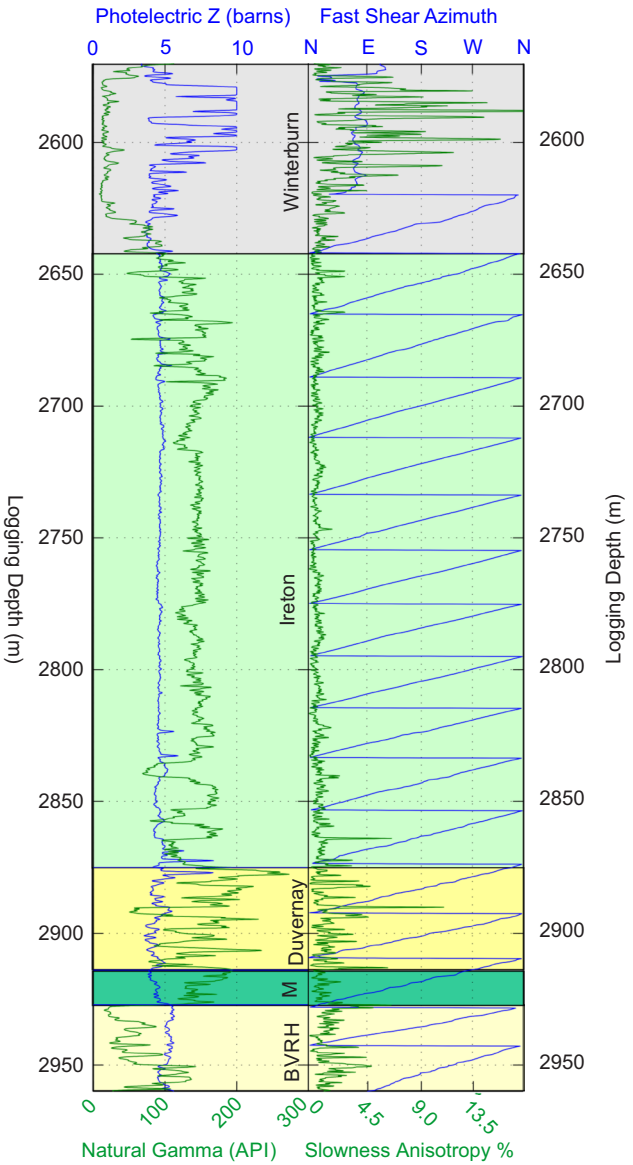

Figure 4 Geology and logs from *02-17-043-04 W5*. Generalized stratigraphy delineated by colour includes the Winterburn Group (dolomites and anhydrite), the Ireton Formation (calcareous and grey-green shales), the target Duvernay Formation (bituminous and calcareous shales), the Majeau Lake Formation (M) (shale), and the Beaverhill Lake Group (limestone and shale). The left panel contains the standard natural gamma radioactivity log and the photoelectric effect log. The right panel shows two attributes derived from the dipole sonic log of the direction of the fast shear wave and the "slowness-based anisotropy".

Table 1 Sample composition

	X-ray Diffraction Analysis									Dry Combustion		
Sample	Quartz	Calcite	Muscovite	Pyrite	Kaolinite	Ankerite	Clinochlore	Orthoclase	Epidote	TOC (wt.%)	Kerogen (wt.%)[1]	Sample Depth (m)
2-13										3.86	4.63	2871.65
5-13										3.74	4.49	2875.66
7-13										2.64	3.17	2878.05
10-13										3.83	4.6	2882.88

1. Kerogen weight fraction estimated from TOC values using conversion factor of 1.2 as provided by Tissot and Welte (1978)

Table 2 Petrophysical properties

Sample	Bulk density ρ_b (kg/m^3)	Skeletal density ρ_s (kg/m^3)	Porosity (%)	Avg Pore Diameter (μm)
2-13	2464	2556	3.61	0.042
5-13	2427	2523	3.80	0.022
7-13	2482	2579	3.78	0.029
10-13	2476	2541	2.56	0.167

EXPERIMENTAL SETUP AND INSTRUMENTATION

In this contribution, the degree of anisotropy and dynamic moduli are measured using the ultrasonic pulse transmission method with piezoelectric ceramic elements. This method has been extensively used to estimate the velocities in geologic material at ultrasonic frequencies.

Core samples (Fig. 6a) were trimmed into a prism-like geometry where the opposing faces allow for wave propagation along the x_1- and x_3-axes well as at an off-axis angle 45° from the bedding plane. This configuration, adapted from Wong *et al.* (2008), allows us to reduce the heterogeneity issues of taking measurements of separate samples taken from the same core; the propagation paths of the different waves all intersect. Each opposing face on the core configuration is grounded parallel to better than 0.1 mm and polished with fine sandpaper to ensure proper adhesion of the piezoelectric elements and strain gauges. For the same reason, samples were vacuum dried at 65 °C as not to compromise the integrity of the bonding agents used to attach the components.

Lead zirconate titanate (PZT) elements with a resonance frequency of 1 MHz are glued directly on to the surface of each face and foil strain gauges oriented parallel and perpendicular to the bedding (Fig. 6b). The sample is then coated with a non-conductive urethane compound in order to test the sample under jacketed conditions.

Experimental setup for the dynamic measurements consists of a pulser/receiver system, a digital oscilloscope, a digitizer, and a pressure vessel (Fig. 7). The pulser repeatedly applies a fast-rise time voltage step to drive the transmitting ceramic. The subsequent pulse propagates through the material as an elastic wave and is converted to a voltage by the receiver transducer. The signal then passes through an 8-bit digitizer before being recorded by the digital oscilloscope at a rate of 10 ns/sample. A LabVIEW® program displays and stacks each signal to produce an averaged waveform in order to reduce electrical and random noise. Detailed example of three waveforms (Fig. 8) highlights the initial RF noise arising from the activation pulse but with a clear and strong (~2-V peak-to-peak) waveform transmitted in all cases. There is no ambiguity in picking the first amplitude extremum in these images. These waveforms also point to an additional advantage of the geometry that consists of relatively large aperture transmitters and receivers directly facing one another. First, the contamination of the signal by "parasitic" arrivals is diminished because directionality effects are minimized. These can be quite problematic when transmitters and receivers do not face one another such that both elements' directionalities are not optimally aligned. Indeed, Mah and Schmitt (2001a, b) exploited the directionality effects to obtain profiles of shear wave modes by using the stronger shear modes radiated at oblique angles by small-aperture P-mode transducers as part of their inversion for the phase velocities in an orthorhombic solid. These parasitic modes cannot be eliminated but are

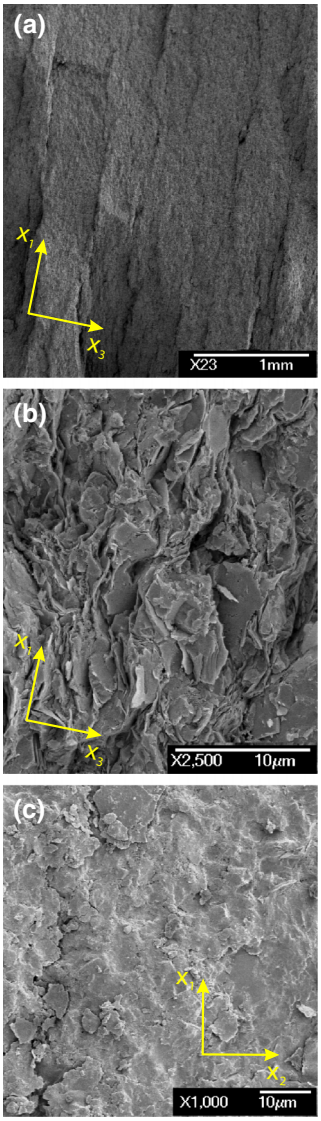

Figure 5 Scanning electronic microscope images of Sample 5-13 with (a) 23 times magnification along x1 highlighting the bedding planes, (b) 2500 times magnification from the same view showing layering of illite grains subparallel to bedding planes, and (c) 1000 times magnification looking down on to bedding planes along x_3.

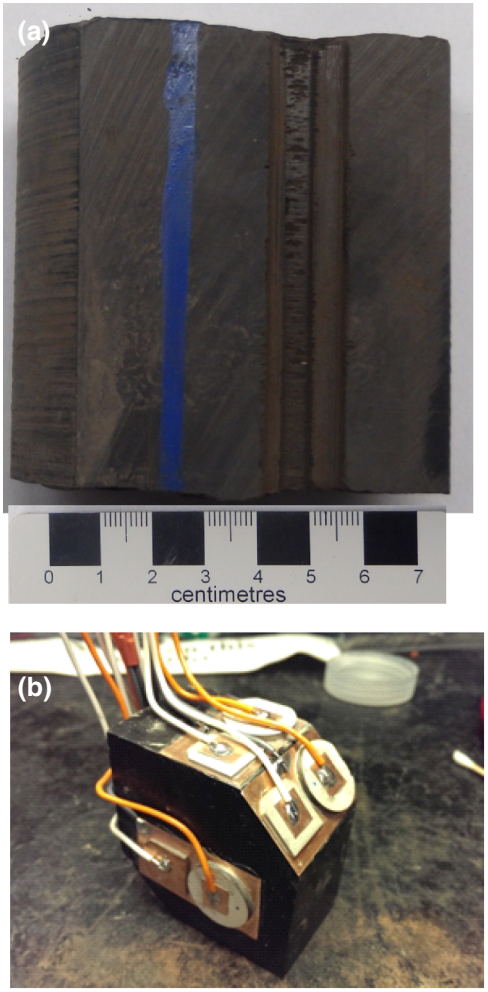

Figure 6 (a) Section of black calcareous shale core from *02-17-043-04 W5* prior to machining. (b) Sample 5-13 before application of urethane compound complete with piezoelectric elements, electrodes, and strain gauges (not shown).

greatly reduced by the geometry used here. Techniques that employ smaller aperture transducers that are not aligned with one another will have waveforms that will be influenced by directionality effects that can cause problems for interpretation of the different shear wave modes, particularly at oblique angles where one expects significant generation of longitudinal waves.

Calibration of the PZT transducers is necessary as there is a slight delay between the excitation and the waveform's first amplitude maximum. For the calibration, PZT crystals (compressional and shear-mode) are mounted on to the flat end of a set of Aluminium 6061-T6 cylinders of varying lengths. Similar to the sample measurements, waveforms are averaged over 300 instances and the transit time is picked from the first extremum of the averaged waveform. These values are then plotted as function of the cylinder length and fitted with a linear regression where the slope is equal to the slowness of the propagating ultrasonic wave that gives compressional and shear speeds of 6211 m/s and 3122 m/s, respectively, which are in good agreement with reported values (Christman *et al.* 1971). The non-zero intercept of the equation is equal to the excitation delay of each transducer plus the required time shift

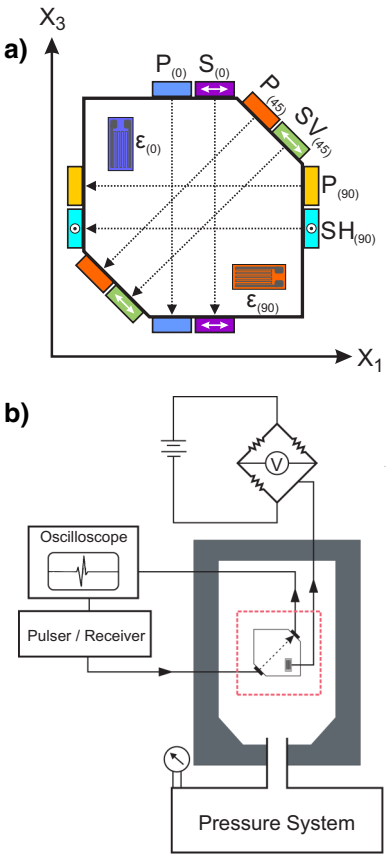

Figure 7 Simplified diagram of (a) Arrangement of ultrasonic piezoelectric ceramic elements on polyhedral sample colour coded for comparison with Fig. 10 and of the two strain gauges colour coded to correlate with Fig. 10. (b) The final experimental configuration including pulser/oscilloscope and Wheatstone bridge arrangements.

to the first arrival, and these time shift values are 1.019 μs and 0.585 μs for the P- and S-wave corrections, respectively.

Samples are subjected to hydrostatic confining pressures up to 90 MPa where, prior to taking measurements, samples are held at a constant pressure for 20 minutes to allow for time-dependent changes due to the new stress conditions. These measurements are initially taken at small pressure increments to target the expected non-linear elasticity of the rocks due to compliant deflects such as cracks, fractures, and grain contacts. As confining pressure is increased, these cracks and fractures close, resulting in a more linearly elastic response. At this stage, measurements are taken at larger pressure intervals.

Static strains are measured through the use of 350-Ω foil strain gauges attached directly to the sample. The changes in resistance due to deformation of the material are generally orders of magnitudes smaller than the changes in nominal resistance of the strain gauge and therefore must be measured with a Wheatstone bridge circuit constructed of precision 350-Ω resistors. DC input voltages of 2.5 V activate the bridge, and the output voltages are measured and recorded using a digital multi-meter facilitated by the same LabVIEW® program. Details of the conversion of the observed unbalanced bridge voltages to strains may be found in Meléndez Martinez (2014).

RESULTS AND DISCUSSION

Wave speeds and dynamic moduli

Four different suites of measurements (hereafter, designated as 2-13, 5-13, 7-13 #1, and 7-13 #2) were made on three of the core samples. The fourth core, sample 10-13, was unsuitable for testing as there was insufficient material to cut into the multi-faced polyhedron, but it still provided petrophysical information that was useful in correcting depths between the logs and the core.

For the sake of completeness, we provide the full suite of waveforms for sample 2-13 (Fig. 9) as an example to observe the shift in the pulse transit times as a function of the confining pressure and quality check for each waveform. The first extremum of each trace appears to be relatively clean and thus puts confidence in our transit time determination. A hysteresis effect is also observed in this figure, but it will be more apparent in the plots of the velocities, elastic constants, and moduli.

In general, the wave speeds observed between the four samples were relatively uniform. It is notable that the speeds measured on 7-13 #1 and 7-13 #2 sampled adjacently to each other in the same piece of core differed at all pressures by less than 100 m/s, indicating the relative homogeneity of the material. Here, only the speeds from samples 5-13 and 7-13 #2 are plotted (as shown in Fig. 10) as, within the set of four, these two differ the most from one another. All of the data for these samples are provided in the electronic supplement. The 45° P-wave transducer on sample 5-13 failed and provided no data. Subsequently, elastic constants that originally required $V_P(45°)$ will instead use the off-axis SV-wave velocity equation (11).

From Fig. 10, we see that, except for $V_{SH}(90°)$, velocities increase with confining pressure and exhibit a hysteresis effect between the pressurization and depressurization cycles. Pressure sensitivity is most pronounced for those wave speeds measured at 0°. In contrast, $V_P(90°)$ modestly increases, whereas $V_{SH}(90°)$ remains nearly constant.

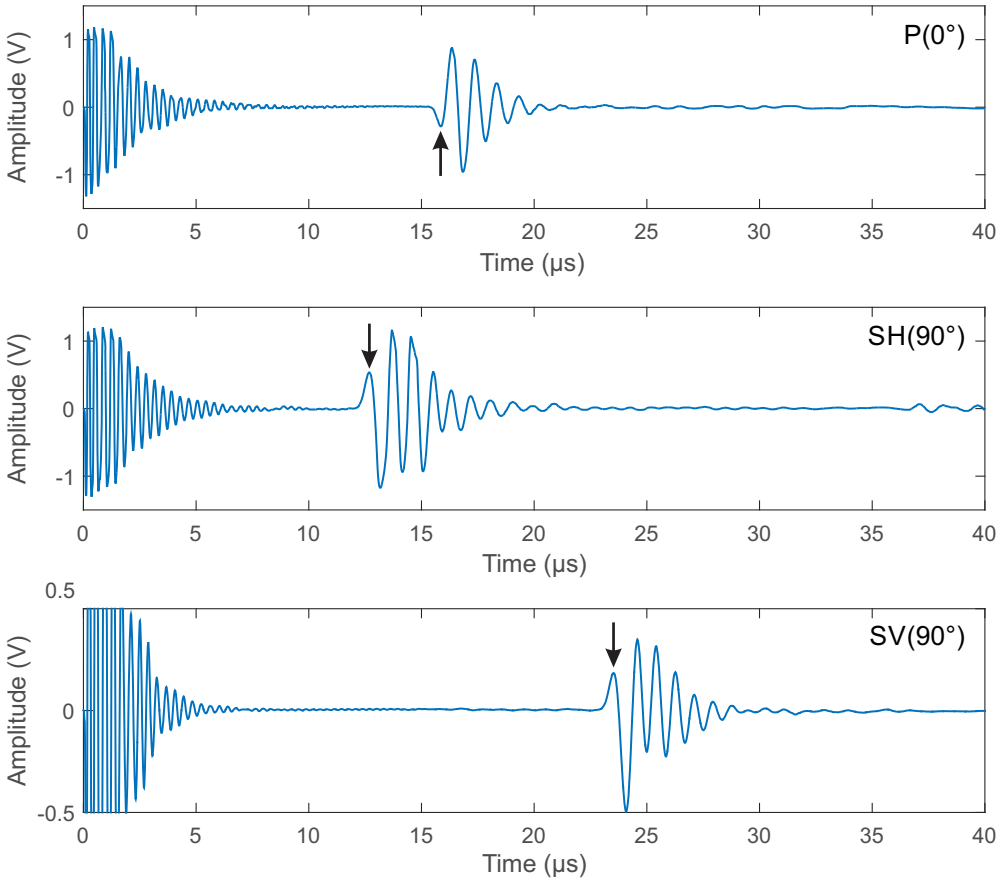

Figure 8 Examples of stacked P-wave signal measured in the x_3 direction, *SH* polarization signal measured in the x_1 direction, and *SV* polarization signal measured at the $\theta = 45°$ direction at 50 MPa of confining pressure and room temperature. Arrow shows time pick at first extremum. The higher frequency oscillations from time $t = 0$ are not signal but are an induction effect in the receiver's circuit arising from the rapid change in voltage that activates the transmitter.

It is useful to consider these observations in terms of the wave polarization. The observation that $V_{SH}(90°)$ remains nearly constant during the entire pressurization is particularly interesting. It suggests that the bedding plane polarized waves are not influenced by small-aspect-ratio, crack-like, pressure-sensitive porosity. At the same time, $V_P(90°)$ does show weak pressure dependence, but this should not be surprising as its polarization and the resulting wave-induced strains will be influenced by both the elastic properties both in and perpendicular to the bedding plane, and its weak pressure sensitivity carries over from the out-of-bedding-plane pressure sensitivities.

Initial observations show that the velocities are consistent with what one would expect from a material with vertical transverse isotropy (VTI) with $V_P(0°) < V_P(45°) < V_P(90°)$ and $V_{SH}(0°) < V_{SV}(45°) < V_{SH}(90°)$. It is interesting to observe, however, that $V_{SH}(90°)$ exceeds $V_P(0°)$ at pressures below 30 MPa in both samples 7-13 #1 and 7-13 #2.

The elastic stiffnesses are calculated directly from the bulk density and the phase velocities of the samples through equations (5)–(11) and plotted as a function of confining pressure (Fig. 11). As the measurements are made under dry conditions, no additional corrections for fluid effects were necessary, and the moduli reported are for the dry frame. From the initial observations, the elastic constants are consistent with the thermodynamic constraints (Auld 1973; Fung 1965) imposed on media of VTI symmetry stemming from the positive definite nature of the strain energy function (Postma 1955). Also included are Young's moduli E_1 and E_3 subsequently determined from the stiffnesses according to equations (A1) and (A2). E_1 substantially exceeds E_3 in all cases. The corresponding dynamic Poisson's ratios calculated from equations (A5)–(A7) are given in Fig. 12. Generally and except at the lowest pressures $\nu_{12} \approx \nu_{13}$, both are significantly smaller than ν_{31}

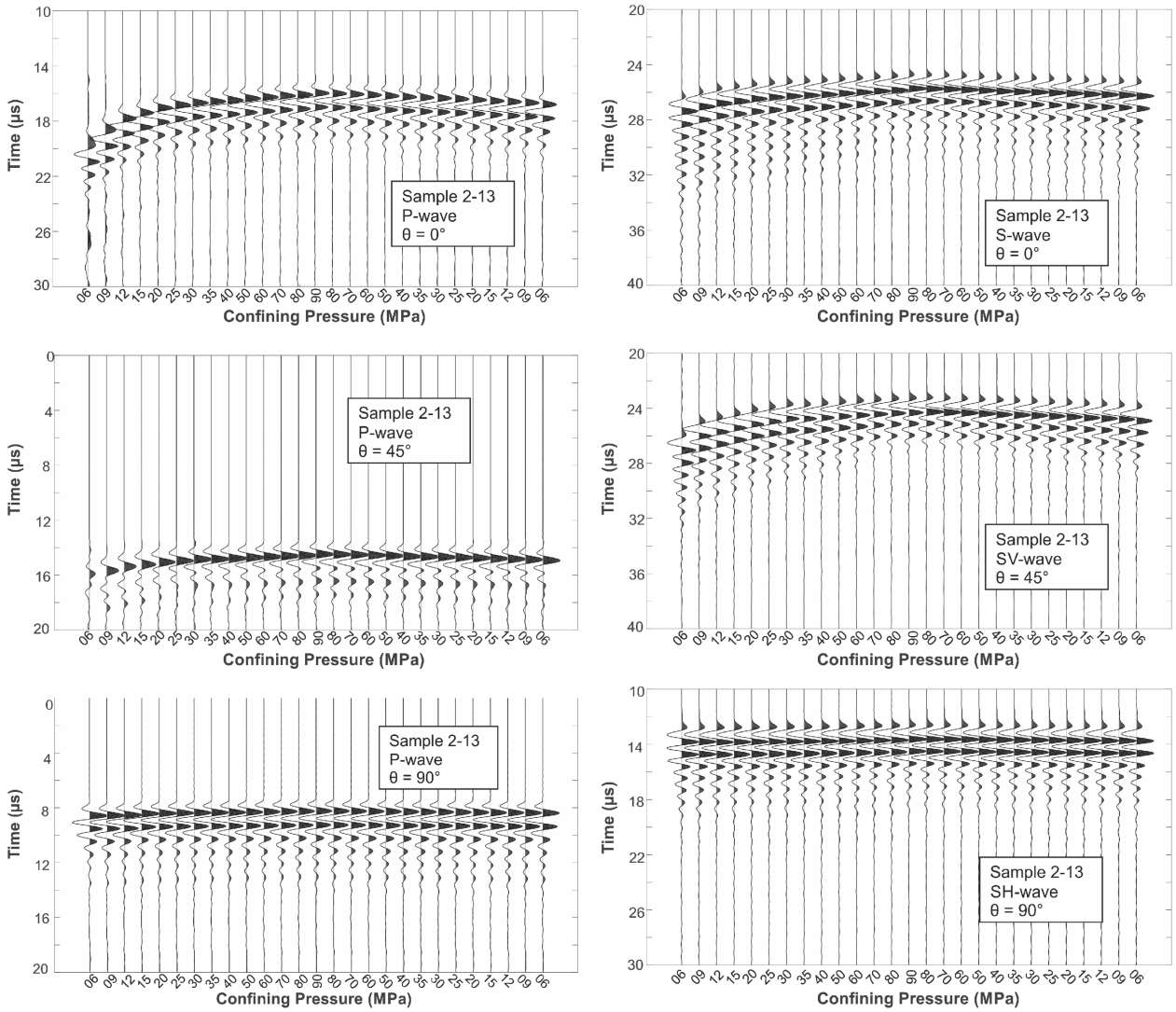

Figure 9 Complete set of observed waveforms for sample 2-13 over range of pressures from 0 MPa to 90 MPa and back.

$$C_{11},\ C_{33},\ C_{44},\ C_{66} > 0. \tag{15}$$

$$C_{11},\ C_{33} > C_{44}. \tag{16}$$

$$C_{11},\ C_{33} > C_{66}. \tag{17}$$

$$C_{33}\,(C_{11} - C_{66}) > {C_{13}}^2. \tag{18}$$

Thomsen (1986) $\boldsymbol{\varepsilon}$, δ, and γ parameters have become important quantitative measures of the anisotropy of a material. These are calculated using equations (A8)–(A10) and shown, including uncertainties, in Fig. 13. Again, 5-13 and 7-13 #2 were chosen as they bound the range of properties seen in the four different samples measured. These results make it clear that these rocks are highly anisotropic with $0.35 < \boldsymbol{\varepsilon} < 0.5$ and $0.3 < \gamma < 0.46$; these correspond to simple anisotropies at the highest confining pressures of 90 MPa. Prior to employing these values for seismic analysis, it would be prudent to assess whether the simplifications remain valid in the analysis of seismic observations within this formation.

Experimental uncertainties were estimated for all variables but only shown for the Thomsen parameters as all others are approximately equal to or smaller than the markers used in the figures. A general propagation of error was used to calculate the variance in each parameter with consideration of the uncertainties in the pulse transmission offset, parallelism of opposing faces, and measurements of physical properties such as bulk density. Limitations in the data acquisition equipment

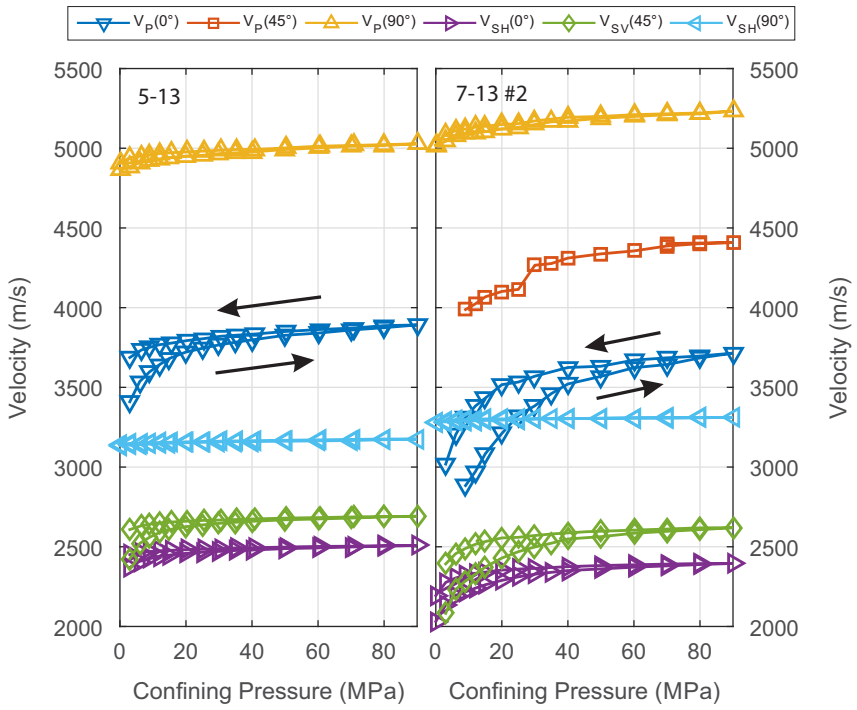

Figure 10 Phase velocity for samples 2-13 and 7-13 #2 plotted as a function of hydrostatic confining pressure. Uncertainties are approximately the size of the markers with arrows showing the evolution of the pressurization and depressurization measurements.

were also considered in the estimates of error although picks in the first arrival were taken to be absolute as the waveforms provided clear distinct points of the first extremum.

Stress–strain relations and static linear stiffnesses

As noted, linear strains were measured both parallel (ε_1) and perpendicular (ε_3) to the bedding plane. In all of these samples, the magnitudes of $\varepsilon_3 > \varepsilon_1$ by factors of 3–6 again indicate that the bedding planes are stiff. Moreover, ε_1 increases almost linearly with pressure and displays little hysteresis upon depressurization (Fig. 14). The grey-shaded area at the top corner of the panels delimits the corresponding linear strain that would be expected for a nonporous isotropic polycrystal of quartz with an adiabatic bulk modulus $K_s = 37.8$ GPa (Schmitt 2015), and although quartz is among the most compressible minerals, the fact that the observed values of ε_1 are close to this do indicate that the bedding planes of these rocks are exceptionally stiff. In contrast, the bedding perpendicular strain ε_3 behaves nonlinearly with pressure. Sample 7-13 #2 has a high strain gradient at low pressures, and its trend becomes increasingly linear at higher pressures, indicating the progressive closure of the crack-like aligned porosity. Sarout and Gueguen (2008b) developed models that are able to incorporate such aligned porosity into an otherwise intrinsically anisotropic medium.

The static linear stiffness of the material is determined by finding the local slope to the strain–pressure curve in Fig. 14. The "tangent" linear stiffnesses were found by fitting an algebraic curve that appropriately fits the observed strain–pressure relationship and then taking its derivative with respect to pressure; the inverse of this slope gives the linear stiffnesses Kl_i as described by equation (11) above (see Melendez Martinez and Schmitt (2015)). These are then compared directly with their dynamic counterparts calculated using equations (13) and (14). It is interesting to note that, in all of the four samples measured, the dynamic and static linear stiffnesses in the bedding plane are nearly equal despite the number of variables necessary to calculate the former. In contrast, those measured perpendicular to the bedding plane diverge. Melendez Martinez and Schmitt (2015) recently found similar behaviour in a series of Cretaceous calcareous mudstones from the Western Canadian Sedimentary Basin but those rocks are less anisotropic.

The directionally dependent differences between the dynamic and static linear stiffnesses may be important. First, perpendicular to the bedding, the two values differ by more than 50% even at the greatest confining pressure. In contrast, along the bedding plane, the two match one another well. This suggests that the degree of difference between the static and the dynamic moduli also varies with direction.

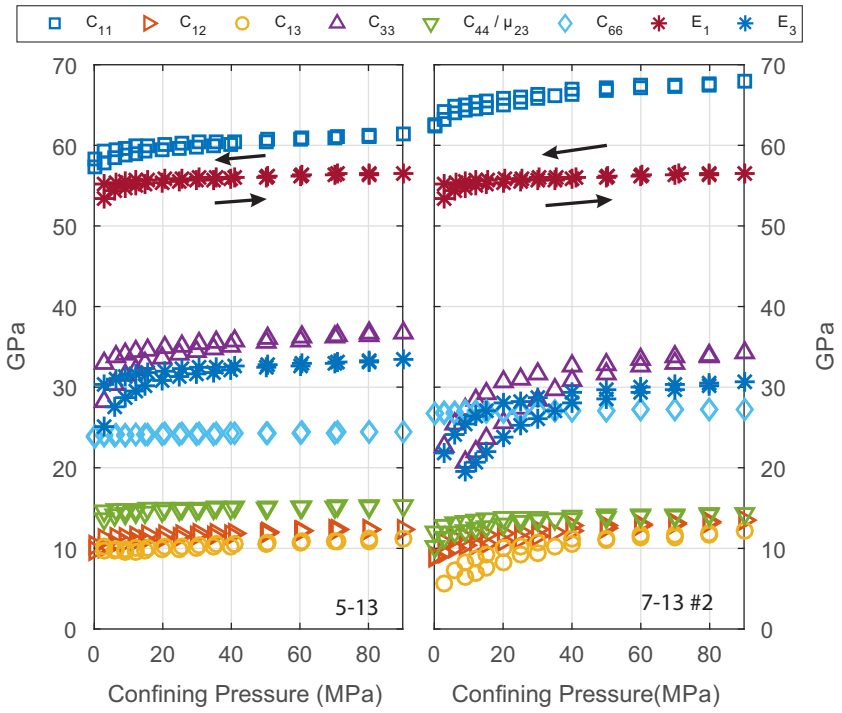

Figure 11 Dynamic elastic stiffnesses and Young's moduli calculated from the observed wave speeds as a function of hydrostatic confining pressure. Arrows show the evolution of pressurization and depressurization measurements. Uncertainties are approximately the size of the markers.

As noted earlier, proper static elastic moduli are necessary for many engineering calculations, but in the absence of core materials they must be estimated from geophysical logs (Asef and Najibi 2013). It has long been known that, at "low" confining pressures typically less than 200 MPa (see review in Simmons and Brace (1965)), the dynamic and static values disagree with one another even in dry rocks (Fjær 2009), as is the case here, where complications related to undrained versus drained and to wave-induced fluid motions cannot act. Comparisons on shales are rare. In an earlier study, Jizba (Jizba and Nur 1990; Jizba 1991) compared static to ultrasonic dynamic measurements on a range of siliclatic rocks, finding that the ratios of the dynamic K_D to the static K_S bulk moduli were great as 5. In the clay-rich rock, this ratio tended to be independent of the confining pressure. Holt *et al.* (2012) reinterpreted earlier measurements of static Young's and dynamic P-wave moduli (i.e., $\rho(V_P)^2$) that upon cross-plotting suggest that, with more data, useful empirical relationships could be developed. Studies that have considered static to dynamic anisotropies explicitly, however, are even rarer. Wong *et al.* (2008) compared static, ultrasonic, and log values for a much more friable and still-wet Cretaceous shale but to confining pressures of only 11 MPa, and in this rock, the dynamic/static Young's moduli ratios differed by factors of 5–6. Although strictly they did not make measurements of the static moduli, Suarez-Rivera *et al.* (2001) briefly reported on a series of measurements on two shales from quasi-static to ultrasonic frequencies and reported that wave speeds over this range would differ by 45%. Hofman (2006) was able to obtain full sets of the elastic stiffnesses at "low" frequencies from 3 Hz to over 1 kHz and compared these to ultrasonic measurements; one of his shales showed significant dispersion, whereas the second did not. Ruiz Pena (1998) also made direct comparisons of linear stiffnesses on a suite of dolomitized shales from Venezuela with the dynamic easily exceeding the static in all cases. More recently, Mbia *et al.* (2014) made ultrasonic and strain measurements on oriented cylinders taken from Jurassic shales cored from the Norwegian–Danish Basin over depths from 1000 m to 4600 m. Their samples were subject to uniaxial loading to 25 MPa while maintaining a constant ratio of 0.38 between the uniaxial stress and the biaxial side pressures. Their static compressibilities always exceeded those determined dynamically except early in the depressurization stage.

Comparison between these many studies is complicated by the fact that they have all been made on a wide variety of "shales", i.e., that some are under dry and others are in full saturation, and at a wide range of triaxial states of stress. The one common element in all is that, generally, dynamic moduli exceed static moduli regardless of direction. In our four

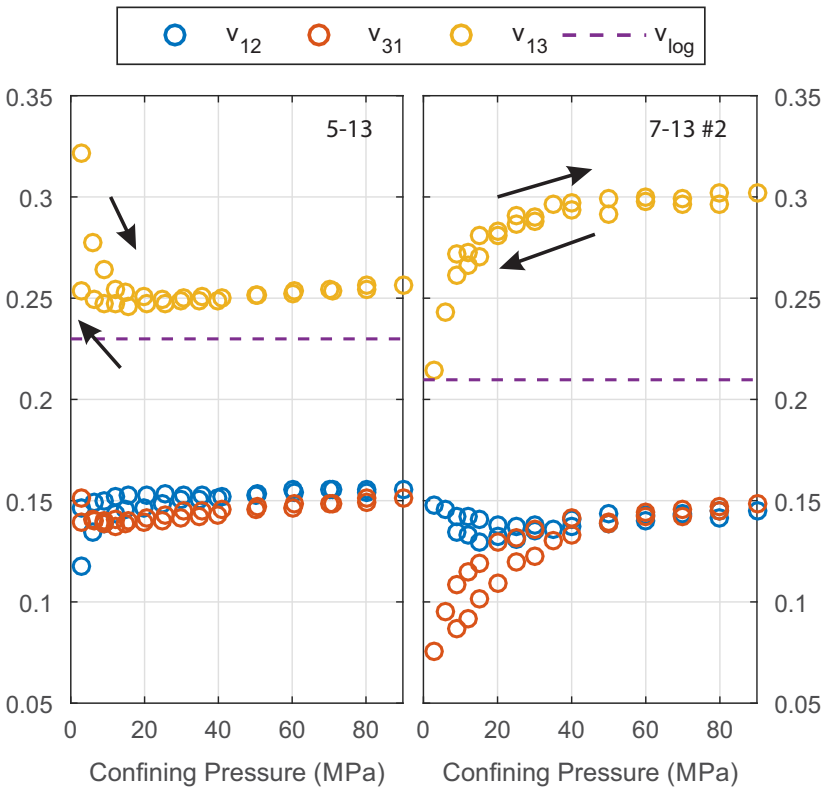

Figure 12 Dynamic Poisson's ratios as a function of hydrostatic confining pressure. Arrows show the evolution of pressurization and depressurization measurements. Uncertainty is approximately the size of the markers.

Duvernay samples, as well as the less anisotropic ones measured by Melendez Martinez and Schmitt (2015), the ratio $R = Kl_i(dynamic)/Kl_i(static)$ critically depends on the direction. This R is always > 1.5 in the direction perpendicular to the bedding planes. This contrasts with the other observations in sandstones and shales in which the value $R \sim 1$ only upon the initial depressurization of the material (e.g., Mbia *et al.* (2014)). The recent study of Holt *et al.* (2015a) too is of interest in this context. They measured the full set of elastic constants on Mancos (8% porosity, 20%–25% clay), Pierre (25% porosity, 40%–60% clay), and Field (10% porosity, 50%–55% clay) shale samples using ultrasonic pulse transmission, strain, and low-frequency forced oscillation methods. The finding for these rocks is that the ultrasonic dynamic moduli exceeded the static moduli in all cases but that the low-frequency moduli reasonably matched the static moduli. In contrast, within this current study, R is always ~ 1 within the bedding plane regardless of whether the sample is in a pressurization or a depressurization cycle. One needs to take care with a direct comparison between these two studies. Their shales contain substantially more clays that the Duvernay Formation material. The Duvernay clays too are non-swelling illite and kaolinite. Holt and coworkers do not report on the kinds of clay, but Pierre shale, for example, can contain considerable proportions of montmorillonite (Schultz *et al.* 1980) and it is possible that the dispersive effects are greater through such materials. Certainly, Wong *et al.* (2008) report large directional variations in attenuation (which is related to dispersion) in earlier studies on wet samples of Colorado shale from Alberta. This anisotropy to R will further complicate attempts to predict the static moduli from geophysical seismic or log wave speeds.

One final issue rests here with the fact that this study is carried out under conditions of hydrostatic pressure while most studies are carried out subject to triaxial states of stress. While the mean stress within the sample must certainly remain as a uniform pressure, the thin-section and SEM images do show that the material's structure is heterogeneous at microscopic scales. As such, we expect that stress concentrations will arise in the vicinity of such structural irregularities. This may partly explain the hysteresis in strains and wave speeds upon depressurization that has long been known. What is anomalous in this study, however, is the lack of significant hysteresis for those deformations of bedding parallel strain

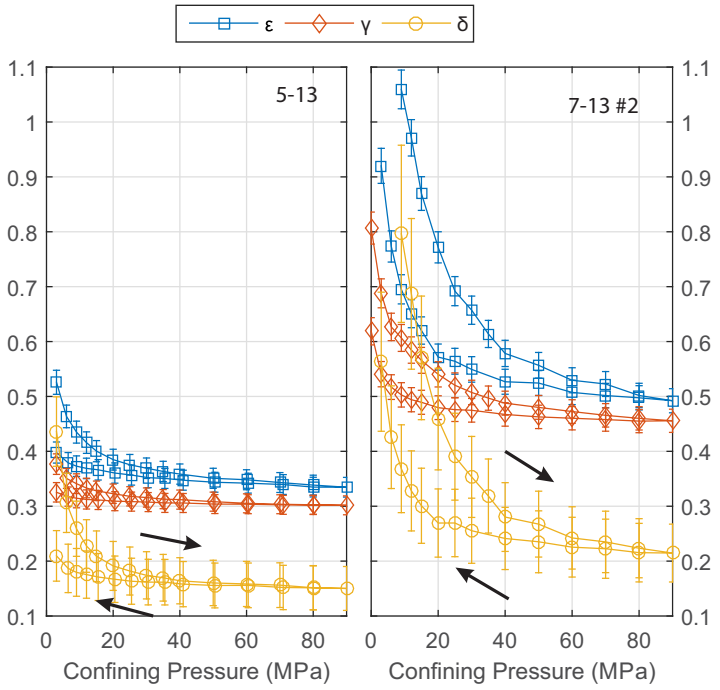

Figure 13 Thomsen (1986) anisotropy parameters ε, δ, and γ calculated from the dynamic elastic stiffnesses.

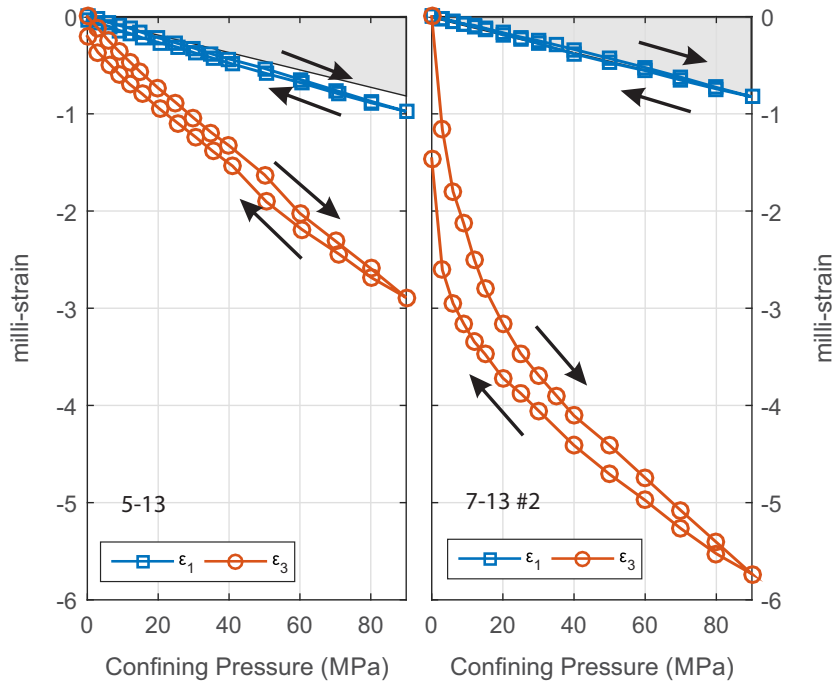

Figure 14 Strains measured perpendicular and parallel to bedding as a function of hydrostatic confining pressure. Uncertainties are smaller than the marker. Arrows show the evolution of the pressurization and depressurization measurements. The grey-shaded area delimits the linear strain that would be expected on a nonporous isotropic quartz polycrystal for purposes of comparison.

and $S_H(90°)$ wave speeds that indicate a lack of crack-like porosity oriented obliquely to the bedding. This suggests that the easily compressible, small-aspect-ratio porosity in this material is dominantly aligned with the horizontal beds. Such preferential structures have been anticipated in the modelling of Sarout and Gueguen (2008b) for shales and were necessary to explain the seismic field observations over a thick biotite schist by Schijns *et al.* (2012).

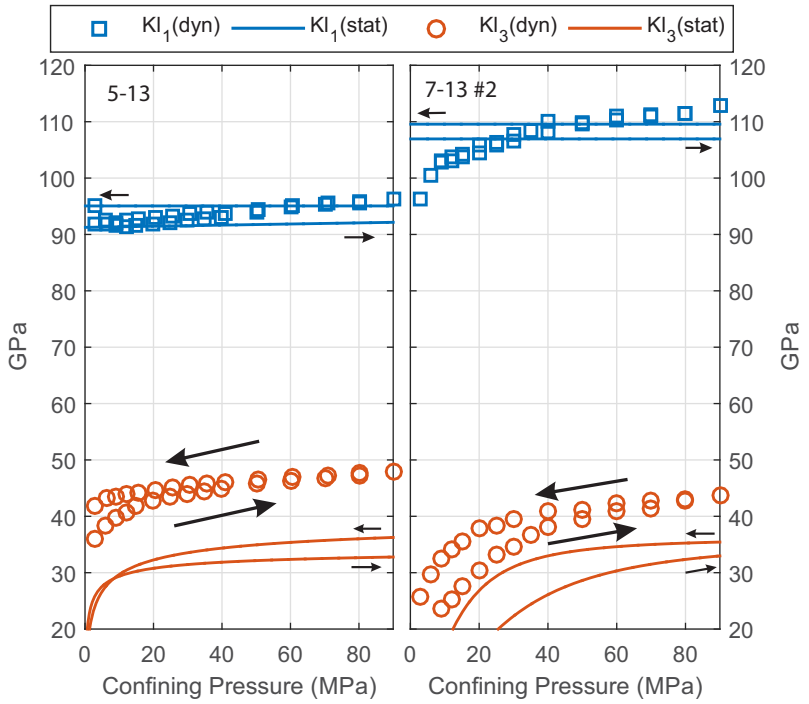

Figure 15 Direct comparison of the strain-derived static (stat) and wave speed-derived dynamic (dyn) linear stiffnesses plotted as a function of hydrostatic confining pressures. Arrows show the evolution of the pressurization and depressurization measurements.

Core to log comparison

An extensive set of geophysical logs was acquired by the operator immediately after drilling of this well, and we are able to obtain these logs through publicly accessible databases; *as provided* directly from the field observations, we do not have access to any subsequently processed log information. Despite this, some borehole data are available that can be compared with the laboratory measurements (Fig. 16). Note that the core depths in Table 1 were shifted downwards 5.55 m to account for incomplete core recovery and differences between the driller's and geophysical log depths; once this shift was effected, the core to log densities agreed well except for sample 5-13, which is noticeably less dense. We do not know the reason for this discrepancy, but it may simply be due to heterogeneity within the formation. Again, we do not know if the density log was in any way corrected for mineralogic content or potential mudcake nor do we have access to the density error log.

The only compressional log available is DT4P, i.e., the compressional wave slowness obtained from the monopole source, and this is the line in the right panel in Fig. 16 where it is directly compared with the values of the wave speed in the different directions. These ultrasonic measurements appear as horizontal lines that represent the full range of values measured over the confining pressure range from 0 MPa to 90 MPa. The results from sample 7-13 #1 are not shown as they are largely similar to those for 7-13 #2. Except for sample 5-13, laboratory $V_P(90°)$ intersects the log-derived curve. In contrast, both $V_P(45°)$ and $V_P(90°)$ substantially exceed log V_P. This is to be expected because, assuming that the borehole remains vertical, the sonic logs are enforced by geometry to provide V_P perpendicular to the bedding plane.

There are more shear wave speed measurements available from the logs and three are given in Fig. 16 and include V_S derived from the transit times of the: (i) monopole source (black line) and (ii) DT1 and DT2, i.e., the two measurements from the upper to the lower dipole transducers and vice versa; these are delimited by the thickness of the green line. Again, except for sample 5-13, the range of laboratory observed $V_S(0°)$ intersects these log-derived V_S curves. As with V_Ps, this is also expected as the polarizations provided by the vertically propagating directly arriving shear waves, regardless of whether a monopole or a dipole source is used, will be parallel to the bedding plane as is the case for $V_S(0°)$. The range of observed $V_S(45°)$ also intersects the log V_S but only at the lowest confining pressures; at higher confining pressures, the values significantly differ. $V_S(90°)$ is always much larger than the log V_S.

This matching is encouraging, but some care should be taken with the interpretation particularly with regard to *in situ* conditions (fluid saturation state, *in situ* stress, pore pressure,

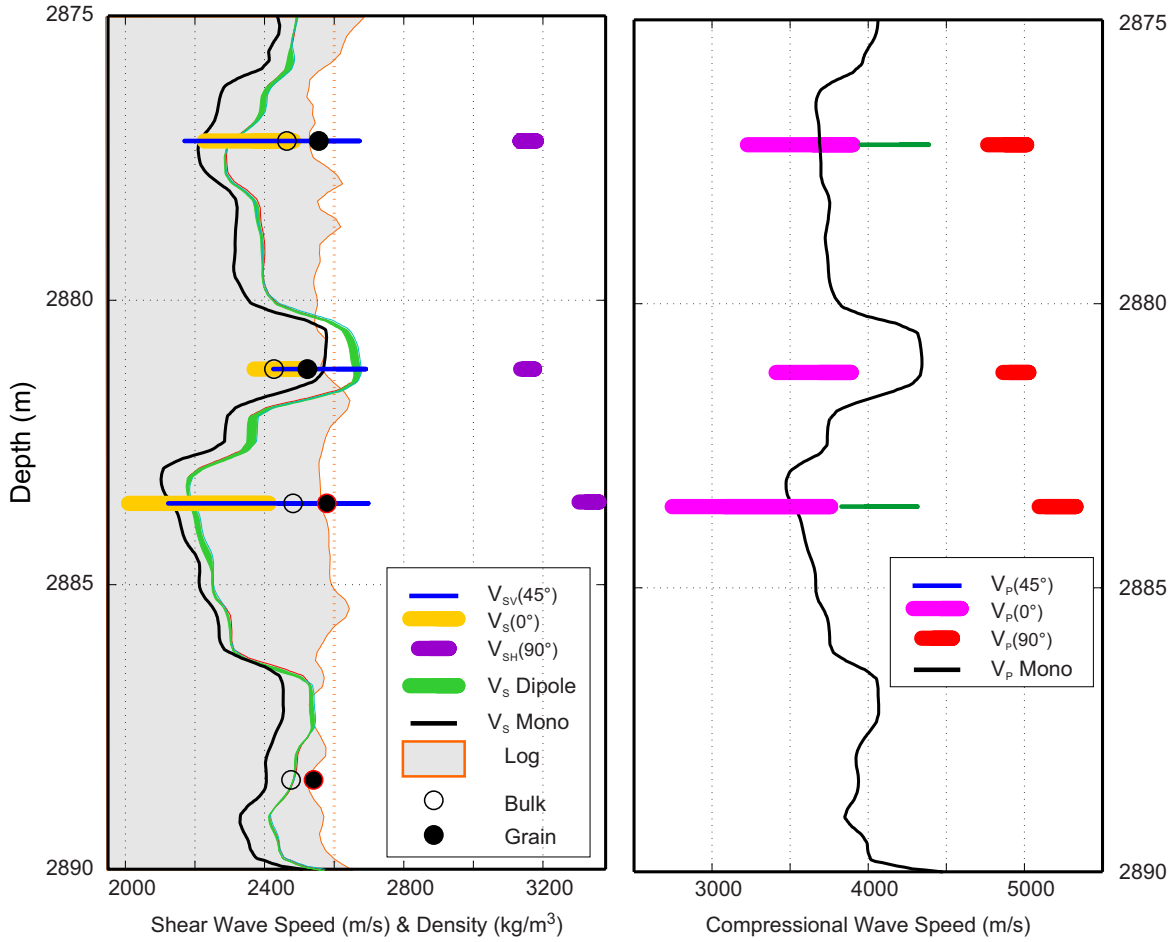

Figure 16 Comparison of log and laboratory wave speeds. Left panel: Red-outlined grey area shows standard $\gamma - \gamma$ density log with corresponding (shifted) laboratory determinations of the dry bulk (open circle) and grain (filled black circle) densities. The green zone bounds the simultaneous S-wave measurements provided by the lower and upper dipoles. The black line is the S-wave speed given from the Δt measurement of the shear wave in from the monopole source. The blue, gold, and purple lines illustrate the range of values of $V_S(45°)$, $V_{SV}(45°)$, and $V_{SH}(90°)$ obtained during pressurization. Right panel: The black line is the P-wave speed given from the Δt measurement of the compressional wave from the monopole source. The green, magenta, and red lines illustrate the range of values of $V_P(45°)$, $V_P(0°)$, and $V_P(90°)$ obtained during pressurization. Line thicknesses are varied only to allow for comparison and have no meaning in themselves.

and temperature), sample heterogeneity and preparation, and the differences between the monopole and the dipole sonic log speeds. As such, it is a useful exercise to determine the confining pressure at which the laboratory and log wave speeds would be equal, the idea being that, barring dispersive effects, the wave laboratory wave speeds could indicate the *in situ* conditions. Taken at face value, the results of this comparison (Table 3) would predict *in situ* stresses of no more than 40 MPa with some of the predicted values approaching zero. The estimated overburden effective stress ranges from 21 MPa to 27 MPa. While this is close to the depressurization V_P values for samples 7-13 #1 and 7-13 #2, the comparison is relatively good. However, it is not known to what degree the differences may arise from dispersion between the ultrasonic and the sonic log frequencies, and this will require additional study (Suarez-Rivera *et al.* 2001). The wave speeds measured at the greatest pressure all exceed those observed from the sonic logs and this at least suggests that some care may need to be taken to account for effective pressure variations when one attempts to determine velocity dispersion.

Implications of stress insensitivity in the bedding plane

It has been long known that the physical properties of most rocks depend nonlinearly on confining stress with this behaviour attributed to the progressive closure of compressible

Table 3 Laboratory confining pressure at which log and laboratory wave speeds match

			Sample Pressure	
Sample	Log VP (m/s)	Log VS (m/s)	Pressurization (MPa)	Depressurization (MPa)
2-13	3689		23	3
		2309	5	NA
5-13	NA		NA	NA
		NA	NA	NA
7-13 #1	3524		40	19
		2192	8	0
7-13 #2	3524		40	20
		2192	6	0

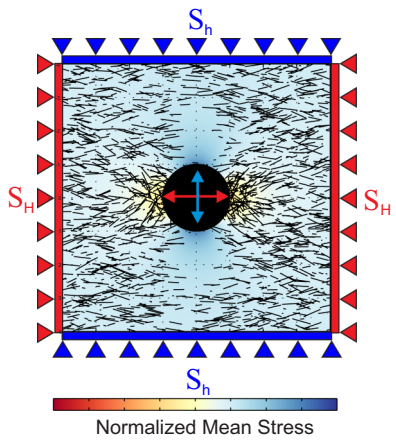

Figure 17 Illustration of the effect of the concentration of the horizontal principal compressions S_H and S_h on the opening and closing of vertical cracks around the borehole. After Fig. 9c of Schmitt *et al.* (2012) with permission granted from Elsevier.

crack-like pores. A corollary manifestation of this nonlinearity is that application of deviatoric stress states induces anisotropy, a topic that has generated a great deal of interest and many literature works in the seismological community based on studies in the laboratory (e.g., Nur and Simmons (1969) and Gorbatsevich and Kovalevskiy (2015)), theoretical analyses (e.g., Sayers and Kachanov (1995); Johnson and Rasolofosaon (1996); and Collet *et al.* (2014)), and in the field (e.g., Crampin (1981); Oda, Yamabe, and Kamemura (1986); Schijns *et al.* (2012); and Shelley *et al.* (2014)). This effect is particularly interesting around a vertical borehole drilled through a formation subject to differing maximum and minimum horizontal compressions S_H and S_h, respectively, as their concentration around the borehole results produces a cyclical pattern of opening and closing of microcracks around the borehole, as illustrated in Fig. 17. These stress concentrations have been shown in the laboratory (Winkler and D'Angelo 2006; Winkler 1996; Fang *et al.* 2013; Hsu *et al.* 2011) and field (Balland and Renaud 2009) to induce considerable azimuthal variations in the compressional and shear wave speeds. These azimuthal variations are also referred to as an "anisotropy", but while it is related to the formation anisotropy due to mineral, crack, and fracture alignment, layering, or *in situ* stress, one must be aware that stress concentrations contribute to these additional changes in the material properties around the borehole (Plona *et al.* 2002). Specialized sonic logging tools that incorporate orthogonal dipole sources (e.g., Sinha, Kane, and Frignet (2000) and Tang and Cheng (2004)) may be used to find the azimuths at which the fastest and the slowest shear waves propagate, yielding the S_H and S_h directions, respectively (Schmitt, Currie, and Zhang 2012).

Such changes, however, are predicated on the existence of compliant crack-like porosity that can be closed by the applied compressions. Here, the relevant laboratory observations are that $V_{SH}(90°)$ is nearly insensitive to confining pressure, that $V_P(90°)$ is only weakly so, and that $\boldsymbol{\varepsilon}_1$ linearly increases with pressure and has little hysteresis upon depressurization. Melendez Martinez and Schmitt (2015) have suggested that this insensitivity to stress would reduce any stress-induced anisotropy. Returning to the logs in Fig. 4, the fast shear wave direction (blue line in the right track) is indeterminate and the slowness-based anisotropy (green line in the right track) is typically $< 1\%$ through the shale formations below 2642 m. At face value, one could interpret this as indicating a nearly uniform state of horizontal stress. However, abundant evidence in the region from the existence of drilling-induced tensile fractures in borehole image logs and focal plane solutions indicating strike-slip indicates that S_H cannot be equal to S_h in this area. The lack of stress sensitivity in the horizontal plane provides a possible explanation for the inability of the fast and slow shear waves to indicate the stress directions. More generally, this may also provide a rationale for Tang and Cheng (2004) observation that the fast shear waver directions cannot be reliably found in shale formations.

CONCLUSIONS

All four samples of calcareous shale from the Duvernay Formation are strongly anisotropic with both simple dynamic anisotropies A_P and A_S ranging between 25% and 35% at

the highest confining pressure of 90 MPa. The sensitivity of the samples to pressure is also highly dependent on direction. Strains and wave speeds measured perpendicular to the bedding direction are nonlinearly dependent upon confining pressure indicative of small-aperture crack-like pores. In contrast, strain measured parallel to bedding increases linearly governed by stiffnesses similar to that expected for a nonporous isotropic quartz composite. Wave speeds in this direction also show little pressure sensitivity. This also translates into an anisotropy of the ratio between the dynamic and the static moduli expressed here as linear stiffnesses. At the highest pressures, the dynamic linear stiffnesses *perpendicular* to bedding exceed the corresponding static stiffnesses significantly. However, somewhat unexpectedly, within the bedding plane, these nearly match.

Ideally, one would like to be able to predict the *in situ* static moduli necessary for engineering purposes from proxy measurements from sonic logs. We found that the speeds of the waves measured perpendicularly to the bedding plane do match the sonic log values particularly once the effective stress is considered. Consequently, one could, in principle, use some empirical relation between the observed dynamic and the static moduli to make a prediction. However, this prediction becomes suspect because of the directional differences in the sensitivity of the moduli to stress. The lack of horizontal stress dependence has implications for the analysis of dipole sonic logs for stress directions; this may explain the degeneracy of the fast shear directions through these calcareous mudstone formations. This suggests that care may need to be taken in the interpretation of seismic azimuthal amplitude versus offset data for stress directions over such formations.

We have not attempted to model the pressure-dependent elastic behaviour. However, there are likely two primary governing factors suggested from the scanning electronic microscope images. These show small aspect ratio "crack-like" pores primarily oriented parallel to the bedding planes. This is consistent with the nonlinear increases in strain and wave speeds perpendicular to this direction. Second, the images also shows strong orientations of the well-bonded phyllitic minerals into tabular sheets, and these features likely are able to support considerable horizontal load. As such, modelling of this behaviour is likely premature until a better understanding of both the character of the porosity and the preferential alignment of the constituent minerals is available. That said, application of models such as those developed by Sarout and Gueguen (2008bb) could reveal additional information on the structure of the pore space in such rocks. Furthermore, as has been done in most previous studies, we assume that our measured values are phase (plane wave) speeds, and if this is not completely, the case then the measurements made at 45° and hence the determined values of C_{13} may be suspect. We believe that this can only be answered properly by a full numerical simulation that will incorporate material properties and transducer apertures. However, the unexpected agreement in all of the cases between the dynamic and static linear stiffnesses suggests that any errors introduced by ignoring the beam propagation are small.

These rocks are highly anisotropic, and they have complex stress-dependent behaviour. Its significance for reflection and microseismic seismology, for stress concentration, and for the risk of induced seismicity is currently being explored.

ACKNOWLEDGEMENTS

Funds for this work were obtained through the Geothermal Studies Section of the Helmholtz-Alberta Initiative.

REFERENCES

Aghighi M.A. and Rahman S.S. 2010. Horizontal permeability anisotropy: Effect upon the evaluation and design of primary and secondary hydraulic fracture treatments in tight gas reservoirs. *Journal of Petroleum Science and Engineering* **74**, 4–13.

AGS. 2015. Alberta Earthquake Studies Project. Vol. 2015.

Amadei B. 1996. Importance of anisotropy when estimating and measuring in situ stresses in rock. *International Journal of Rock Mechanics and Mining Sciences & Geomechanics Abstracts* **33**, 293–325.

Anderson S., Rokosh C.D., Pawlowicz J.G., Berhane H. and Beaton A.P. 2010. Mineralogy, Permeametry, Mercury Porosimetry, Pycnometry and Scanning Electron Microscope Imaging of Duvernay and Muskwa Formations in Alberta: Shale Gas Data Release. In: *Open File Reports,* ERCB/AGS Open File Report 2010–02, p. 67. Alberta Geological Survey.

Asef M.R. and Najibi A.R. 2013. The effect of confining pressure on elastic wave velocities and dynamic to static Young's modulus ratio. *Geophysics* **78**, D135–D142.

Auld B.A. 1973. *Acoustic Fields and Waves in Solids*. Wiley-Interscience Publication.

Balland C. and Renaud V. 2009. High-resolution velocity field imaging around a borehole: Excavation-damaged zone characterization. *Geophysics* **74**, E223–E232.

Birch F. 1961. Velocity of compressional waves in rocks to 10 kilobars: 2. *Journal of Geophysical Research* **66**, 2199–2224.

Blum T.E., Adam L. and van Wijk K. 2013. Noncontacting benchtop measurements of the elastic properties of shales. *Geophysics* **78**, C25–C31.

Brace W.F. 1965. Some new measurements of linear compressibility of rocks. *Journal of Geophysical Research* **70**, 391–398.

Cheadle S.P., Brown R.J. and Lawton D.C. 1991. Orthorhombic anisotropy: A physical seismic modeling study. *Geophysics* **56**, 1603–1613.

Chenevert M.E. and Gatlin C. 1965. Mechanical anisotropies of laminated sedimentary rocks. *Society of Petroleum Engineers Journal* 67–77.

Cheng C.H. and Johnston D.H. 1981. Dynamic and static moduli. *Geophysical Research Letters* **8**, 39–42.

Cholach P.Y. and Schmitt D.R. 2006. Intrinsic elasticity of a textured transversely isotropic muscovite aggregate: Comparisons to the seismic anisotropy of schists and shales. *Journal of Geophysical Research: Solid Earth* **111**.

Christman D.R., Isbell W.M., Babcock S.G., McMillan A.R. and Green S.J. 1971. Measurements of dynamic properties of materials, Vol. III 6061-T6 Aluminum. p. 156.

Ciccotti M. and Mulargia E. 2004. Differences between static and dynamic elastic moduli of a typical seismogenic rock. *Geophysical Journal International* **157**, 474–477.

Clarkson C.R., Solano N., Bustin R.M., Bustin A.M.M., Chalmers G.R.L., He L. *et al*. 2013. Pore structure characterization of North American shale gas reservoirs using USANS/SANS, gas adsorption, and mercury intrusion. *Fuel* **103**, 606–616.

Collet O., Gurevich B., Madadi M. and Pervukhina M. 2014. Modeling elastic anisotropy resulting from the application of triaxial stress. *Geophysics* **79**, C135–C145.

Crampin S. 1981. A review of wave motion in anisotropic and cracked elastic-media. *Wave Motion* **3**, 343–391.

Dewhurst D.N. and Siggins A.F. 2006. Impact of fabric, microcracks and stress field on shale anisotropy. *Geophysical Journal International* **165**, 135–148.

Fang X.D., Fehler M., Zhu Z.Y., Chen T.R., Brown S., Cheng A. *et al*. 2013. An approach for predicting stress-induced anisotropy around a borehole. *Geophysics* **78**, D143–D150.

Fjær E. 2009. Static and dynamic moduli of a weak sandstone. *Geophysics* **74**, WA103–WA112.

Fung Y.C. 1965. *Foundations of Solid Mechanics*. Prentice Hall.

Gaede O., Karpfinger F., Jocker J. and Prioul R. 2012. Comparison between analytical and 3D finite element solutions for borehole stresses in anisotropic elastic. *International Journal of Rock Mechanics and Mining Sciences* **51**, 53–63.

Gautam R. and Wong R.C.K. 2006. Transversely isotropic stiffness parameters and their measurement in Colorado shale. *Canadian Geotechnical Journal* **43**, 1290–1305.

Gholami R., Rasouli V., Aadnoy B. and Mohammadi R. 2015. Application of in situ stress estimation methods in wellbore stability analysis under isotropic and anisotropic conditions. *Journal of Geophysics and Engineering* **12**, 657–673.

Gorbatsevich F.F. and Kovalevskiy M.V. 2015. Experience in applying the acoustopolarization method for metamorphosed rock samples from the Kola (SG-3), German (KTB-HB) and Finnish (OKU) investigation boreholes. Acta Geodynamica et Geomaterialia **12**, 91–100.

Heng S., Guo Y.T., Yang C.H., Daemen J.J.K. and Li Z. 2015. Experimental and theoretical study of the anisotropic properties of shale. *International Journal of Rock Mechanics and Mining Sciences* **74**, 58–68.

Hofman R. 2006. *Frequency dependent elastic and anelastic properties of clastic rocks*. PhD thesis, Colorado School of Mines, USA.

Holt R.M., Bauer A., Fjær E., Stenebråten J.F. and Szewczyk D. 2015a. Relating static and dynamic mechanical anisotropies of shale. *49th US Rock Mechanics/Geomechanics Symposium*. American Rock Mechanics Association.

Holt R.M., Fjaer E., Stenebraten J.F. and Nes O.M. 2015b. Brittleness of shales: Relevance to borehole collapse and hydraulic fracturing. *Journal of Petroleum Science and Engineering* **131**, 200–209.

Holt R.M., Nes O.M., Stenebraten J.F. and Fjaer E. 2012. Static vs. dynamic behavior of shale. *46th US Rock Mechanics/Geomechanics Symposium*, p. 12. American Rock Mechanics Association.

Homand F., Morel E., Henry J.P., Cuxac P. and Hammade E. 1993. Characterization of the moduli of elasticity of an anisotropic rock using dynamic and static methods. *International Journal of Rock Mechanics and Mining Sciences & Geomechanics Abstracts* **30**, 527–535.

Hsu C.J., Kane M.R., Winkler K., Wang C.Y. and Johnson D.L. 2011. Experiments on stress dependent borehole acoustic waves. *Journal of the Acoustical Society of America* **130**, 1799–1809.

Islam M.A. and Skalle P. 2013. An experimental investigation of shale mechanical properties through drained and undrained test mechanisms. *Rock Mechanics and Rock Engineering* **46**, 1391–1413.

Jaeger J.C., Cook N.G.W. and Zimmerman R.W. 2007. *Fundamentals of Rock Mechanics*, 4th edn. Blackwell.

Jakobsen M. and Johansen T.A. 2000. Anisotropic approximations for mudrocks: A seismic laboratory study. *Geophysics* **65**, 1711–1725.

Jia Q., Schmitt D.R., Moeck I. and Kofman R.S. 2014. Improving borehole instability analysis by investigating the impacts of stress and rock anisotropy. *GeoConvention* 2014, p. 7. Canadian Society of Exploration Geophysicists.

Jin Y., Yuan J., Hou B., Chen M., Lu Y., Li S. *et al*. 2012. Analysis of the vertical borehole stability in anisotropic rock formations. *Journal of Petroleum Exploration and Production Technology* **2**, 197–207.

Jizba D. 1991. Mechanical and acoustical properties of sandstones and shales. PhD thesis, Stanford University, USA, 275 pp.

Jizba D. and Nur A. 1990. Static and dynamic moduli of tight gas sandstones and their relation to formation properties (SPWLA-1990-BB). *31st Annual Symposium*, pp. 1–21. Society of Petrophysicists and Well Log Analysts.

Johnson P.A. and Rasolofosaon P.N.J. 1996. Nonlinear elasticity and stress-induced anisotropy in rock. *Journal of Geophysical Research: Solid Earth* **101**, 3113–3124.

Johnston J.E. and Christensen N.I. 1995. Seismic anisotropy of shales. *Journal of Geophysical Research: Solid Earth* **100**, 5991–6003.

Kaarsberg E.A. 1959. Introductory studies of natural and artificial argillaceous aggregates by sound-propagation and x-ray diffraction methods. *Journal of Geology* **67**, 447–472.

Kawasaki I. and Tanimoto T. 1981. Radiation-patterns of body waves due to the seismic dislocation occurring in an anisotropic source medium. *Bulletin of the Seismological Society of America* **71**, 37–50.

King A. and Talebi S. 2007. Anisotropy effects on microseismic event location. *Pure and Applied Geophysics* **164**, 2141–2156.

King M.S. 1969. Static and dynamic elastic moduli of rocks under pressure. pp. 329–351. American Rock Mechanics Association.

Li J.L., Li C., Morton S.A., Dohmen T., Katahara K. and Toksoz M.N. 2014. Microseismic joint location and anisotropic velocity inversion for hydraulic fracturing in a tight Bakken reservoir. *Geophysics* **79**, C111–C122.

Lokajicek T. and Svitek T. 2015. Laboratory measurement of elastic anisotropy on spherical rock samples by longitudinal and transverse sounding under confining pressure. *Ultrasonics* **56**, 294–302.

Mah M. and Schmitt D.R. 2001a. Experimental determination of the elastic coefficients of an orthorhombic material. *Geophysics* **66**, 1217–1225.

Mah M. and Schmitt D.R. 2001b. Near point-source longitudinal and transverse mode ultrasonic arrays for material characterization. *IEEE Transactions on Ultrasonics Ferroelectrics and Frequency Control* **48**, 691–698.

Mashinsky E.I. 2003. Differences between static and dynamic elastic moduli of rocks: Physical causes. Geologiya i Geofizika **44**, 953–959.

Maxwell S.C., Zhang F. and Damjanac B. 2014. Geomechanical assessment of seismic hazard from hydraulic fracturing. *GeoConvention* 2015, p. 4. Canadian Society of Exploration Geophysicists.

Mbia E.N., Fabricius I.L., Krogsbøll A., Frykman P. and Dalhoff F. 2014. Permeability, compressibility and porosity of Jurassic shale from the Norwegian–Danish Basin. *Petroleum Geoscience* **20**, 257–281.

McLamore R. and Gray K.E. 1967. The mechanical behavior of anisotropic sedimentary rocks. *Journal of Manufacturing Science and Engineering* **89**, 62–73.

Meléndez Martinez J. 2014. *Elastic properties of sedimentary rocks*. PhD thesis, University of Alberta, Canada, 242 pp.

Melendez Martinez J. and Schmitt D.R. 2015. A comparative study of the anisotropic dynamic and static elastic moduli of unconventional reservoir shales: Implication for geomechanical investigations. *Geophysics submitted*, 51 pp.

Miller D., Plumb R. and Boitnott G. 2013. Compressive strength and elastic properties of a transversely isotropic calcareous mudstone. *Geophysical Prospecting* **61**, 315–328.

Nadri D., Sarout J., Bona A. and Dewhurst D. 2012. Estimation of the anisotropy parameters of transversely isotropic shales with a tilted symmetry axis. *Geophysical Journal International* **190**, 1197–1203.

Nara Y., Kato H., Yoneda T. and Kaneko K. 2011. Determination of three-dimensional microcrack distribution and principal axes for granite using a polyhedral specimen. *International Journal of Rock Mechanics and Mining Sciences* **48**, 316–335.

Niandou H., Shao J.F., Henry J.P. and Fourmaintraux D. 1997. Laboratory investigation of the behaviour of Tournemire shale. *International Journal of Rock Mechanics and Mining Sciences* **34**, 3–16.

Nur A. and Simmons G. 1969. Stress-induced velocity anisotropy in rock: An experimental study. *Journal of Geophysical Research* **74**, 6667–6674.

Oda M., Yamabe T. and Kamemura K. 1986. A crack tensor and its relation to wave velocity anisotropy in jointed rock masses. *International Journal of Rock Mechanics and Mining Sciences & Geomechanics Abstracts* **23**, 387–397.

Ong S.H. and Roegiers J.C. 1996. Fracture initiation from inclined wellbores in anisotropic formations. *Journal of Petroleum Technology* **48**, 612–619.

Plona T.J., Kane M.R., Sinha B. and Walsh J. 2002. Evaluating stress-induced anisotropy and mechanical damage from cross-dipole sonic data using dispersion analysis (SPE/ISRM 78233). *SPE/ISRM Rock Mechanics Conference*, p. 6. Society of Petroleum Engineers.

Postma G.W. 1955. Wave propagation in stratified media. *Geophysics* **20**, 780–806.

Rokosh C.D., Lyster S., Anderson S.D.A., Beaton A.P., Berhane H., Brazzoni T. *et al*. 2012. Summary of Alberta's Shale- and Siltstone-Hosted Hydrocarbons. p. 191.

Ruiz Pena F. 1998. *Elastic properties of sedimentary anisotropic rocks*. MSc thesis, Massachusetts Institute of Technology, USA, 132 pp.

Sarout J., Esteban L., Delle Piane C., Maney B. and Dewhurst D.N. 2014. Elastic anisotropy of Opalinus Clay under variable saturation and triaxial stress. *Geophysical Journal International* **198**, 1662–1682.

Sarout J. and Gueguen Y. 2008a. Anisotropy of elastic wave velocities in deformed shales: Part 1—Experimental results. *Geophysics* **73**, D75–D89.

Sarout J. and Gueguen Y. 2008b. Anisotropy of elastic wave velocities in deformed shales: Part 2—Modeling results. *Geophysics* **73**, D91–D103.

Sarout J., Molez L., Gueguen Y. and Hoteit N. 2007. Shale dynamic properties and anisotropy under triaxial loading: Experimental and theoretical investigations. *Physics and Chemistry of the Earth* **32**, 896–906.

Sayers C.M. 2013. The effect of anisotropy on the Young's moduli and Poisson's ratios of shales. *Geophysical Prospecting* **61**, 416–426.

Sayers C.M. and Kachanov M. 1995. Microcrack-induced elastic-wave anisotropy of brittle rocks. *Journal of Geophysical Research: Solid Earth* **100**, 4149–4156.

Schijns H., Schmitt D.R., Heikkinen P.J. and Kukkonen I.T. 2012. Seismic anisotropy in the crystalline upper crust: Observations and modelling from the Outokumpu scientific borehole, Finland. *Geophysical Journal International* **189**, 541–553.

Schmitt D.R. 2015. 11.03 - Geophysical properties of the near surface earth: Seismic properties. In:*Treatise on Geophysics*), 2nd edn (ed G. Schubert, pp. 43–87. Elsevier.

Schmitt D.R., Currie C.A. and Zhang L. 2012. Crustal stress determination from boreholes and rock cores: Fundamental principles. *Tectonophysics* **580**, 1–26.

Schultz L.G., Tourtelot H.A., Gill J.R. and Boerngen J.G. 1980. Composition and properties of the Pierre Shale and equivalent rocks, northern Great Plains region. In: *Professional Paper*.

Shelley A., Savage M., Williams C., Aoki Y. and Gurevich B. 2014. Modeling shear wave splitting due to stress-induced anisotropy,

with an application to Mount Asama Volcano, Japan. *Journal of Geophysical Research: Solid Earth* **119**, 4269–4286.
Simmons G. and Brace W. 1965. Comparison of static and dynamic measurements of compressibility of rocks. *Journal of Geophysical Research* **70**, 5649–5656.
Sinha B.K., Kane M.R. and Frignet B. 2000. Dipole dispersion crossover and sonic logs in a limestone reservoir. *Geophysics* **65**, 390–407.
Sondergeld C.H., Ambrose R.J., Rai C.S. and Moncrieff J. 2010. Micro-structural studies of gas shales (SPE 131771). *SPE Unconventional Gas Conference*, p. 17. Society of Petroleum Engineers.
Sone H. and Zoback M.D. 2013. Mechanical properties of shale-gas reservoir rocks — Part 1: Static and dynamic elastic properties and anisotropy. *Geophysics* **78**, D378–D389.
Suarez-Rivera R., Willson S., Nakagawa S. and Magnar-Ness O. 2001. Frequency scaling for evaluation of shale and mudstone properties from acoustic velocities. *EOS Transactions American Geophysical Union* **82**, 1.
Tang X.M. and Cheng A. 2004. *Quantitative Borehole Acoustic Methods*. Elsevier.
Thomsen L. 1986. Weak elastic anisotropy. *Geophysics* **51**, 1954–1966.
Vahid S. and Ahmad G. 2011. Hydraulic fracture initiation from a wellbore in transversely isotropic rock. *45th US Rock Mechanics/Geomechanics Symposium*. American Rock Mechanics Association.
Vavryčuk V. 2005. Focal mechanisms in anisotropic media. *Geophysical Journal International* **161**, 334–346.
Vernik L. and Liu X.Z. 1997. Velocity anisotropy in shales: A petrophysical study. *Geophysics* **62**, 521–532.
Voigt W. 1928. *Lehrbuch der Kristallphysik (mit Ausschluss der Kristalloptik*). B.G. Teubner.
Wang Z.J. 2002a. Seismic anisotropy in sedimentary rocks, part 1: A single-plug laboratory method. *Geophysics* **67**, 1415–1422.
Wang Z.J. 2002b. Seismic anisotropy in sedimentary rocks, part 2: Laboratory data. *Geophysics* **67**, 1423–1440.
Waters G.A., Lewis R.E. and Bentley D. 2011. *The Effect of Mechanical Properties Anisotropy in the Generation of Hydraulic Fractures in Organic Shales*. Society of Petroleum Engineers.
Winkler K.W. 1996. Azimuthal velocity variations caused by borehole stress concentrations. *Journal of Geophysical Research: Solid Earth* **101**, 8615–8621.
Winkler K.W. and D'Angelo R. 2006. Ultrasonic borehole velocity imaging. *Geophysics* **71**, F25–F30.
Wong R.C.K., Schmitt D.R., Collis D. and Gautam R. 2008. Inherent transversely isotropic elastic parameters of over-consolidated shale measured by ultrasonic waves and their comparison with static and acoustic in situ log measurements. *Journal of Geophysics and Engineering* **5**, 103–117.
Wüst R.A., Nassichuk B.R. and Bustin R.M. 2013. Porosity characterization of various organic-rich shales from the Western Canada Sedimentary Basin, Alberta and British Columbia, Canada. In: *Electron Microscopy of Shale Hydrocarbon Reservoirs*, Vol. **102** (eds W. Camp, E. Diaz, and B. Wawak), pp. 81–100. American Association of Petroleum Geologists.
Zisman W.A. 1933. Compressibility and anisotropy of rocks at and near the Earth's surface. *Proceedings of the National Academy of Sciences of the United States of America* **19**, 666–679.

APPENDIX A

For a transversely isotropic medium, we can define expressions for the dynamic Young's modulus E, bulk modulus K, shear modulus μ, and Poisson's ratio ν as a function of the experimentally determined effective elastic constants

$$E_1 = \frac{4C_{66}\left[C_{33}\left(C_{11}-C_{66}\right)-{C_{13}}^2\right]}{C_{11}C_{33}-{C_{13}}^2}. \tag{A1}$$

$$E_3 = \frac{C_{33}\left(C_{11}-C_{66}\right)-{C_{13}}^2}{C_{11}-C_{66}}. \tag{A2}$$

$$K = \frac{C_{33}\left(C_{11}-C_{66}\right)-{C_{13}}^2}{C_{33}+C_{11}-C_{66}-2C_{13}}. \tag{A3}$$

$$\mu_{23} = C_{44}. \tag{A4}$$

$$\nu_{12} = \frac{C_{12}C_{33}-{C_{13}}^2}{C_{11}C_{33}-{C_{13}}^2}. \tag{A5}$$

$$\nu_{31} = \frac{C_{13}}{C_{11}+C_{12}}. \tag{A6}$$

$$\nu_{13} = \frac{C_{13}\left(C_{11}-C_{12}\right)}{C_{11}C_{33}-{C_{13}}^2}, \tag{A7}$$

where ν_{ij} refers to the negative ratio of transverse strain $\boldsymbol{\varepsilon}_j$ to axial strain $\boldsymbol{\varepsilon}_i$ with a uniaxial stress applied as $\boldsymbol{\sigma}_i$.

Define three dimensionless parameters to describe the anisotropy of a transverse isotropy (TI) medium provided that the anisotropy is weak. These parameters are described by the following equations:

$$\boldsymbol{\varepsilon} = \frac{C_{11}-C_{33}}{2C_{33}}. \tag{A8}$$

$$\gamma = \frac{C_{66}-C_{44}}{2C_{44}}. \tag{A9}$$

$$\delta = \frac{\left(C_{13}+C_{44}\right)^2-\left(C_{33}-C_{44}\right)^2}{2C_{33}\left(C_{33}-C_{44}\right)}, \tag{A10}$$

where $\boldsymbol{\varepsilon}$ and γ are expressions used to quantify the degree of P- and S-wave anisotropies, respectively. Parameter δ can be seen as the anellipticity of the P-wavefront. The deviation of these parameters from zero characterizes the relative strength of anisotropy in the material (Yi-Mou *et al.* 2014). We also define the simpler and more traditional fractional anisotropies,

which are simply the ratio of the difference between the maximum and minimum wave speeds with their average value, in which (Birch 1961) for the P-wave here will be:

$$A_P = \frac{V_P\,(90^\circ) - V_P\,(0^\circ)}{V_P\,(90^\circ) + V_P\,(0^\circ)/2}. \tag{A11}$$

and, for the S_H-wave, is

$$A_S = \frac{V_{SH}\,(90^\circ) - V_S\,(0^\circ)}{V_{SH}\,(90^\circ) + V_S\,(0^\circ)/2}. \tag{A12}$$

Note that, for a TI medium, $V_{SV}(0°) = V_{SV}(90°)$, and calculating its anisotropy in a similar manner would be misleading as $V_{SV}(\theta)$ may show a great deal of variation.

APPENDIX B: QUANTITATIVE ESTIMATION OF STRESS

Here we use publicly available data to estimate *in situ* stress conditions. Borehole *02-17-043-04 W5* was first drilled vertically to 2977 m to provide the log information, and then cemented and re-drilled with a long horizontal leg at depths of 2895 m.

- The vertical stress was estimated from integration of a density log formed as a composite of the data from the study well with those nearby to range between 71.0 MPa and 76.7 MPa.
- $S_h = 74.9 \pm 5.9$ MPa is constrained from the average of the reported instantaneous shut-in pressures from the ten successful hydraulic fracture stimulations. This includes the correction for head pressures as described for the formation pore pressure.
- The formation pore pressure is estimated from an 84-hour monitor pressure build-up test conducted after completion of the hydraulic fracture stimulations with the final *shut-in casing pressure* = 18.089 MPa measured at the surface. Using the last reported fluid density of 1090 kg/m^3, we estimate the head pressure at the depth of the stimulations to be 30.96 MPa, suggesting that the formation pressure is 49.04 MPa. This formation is highly overpressured.
- Taken together, these values suggest that the effective vertical stress for wave speeds is 22 MPa–27 MPa.
- It is useful to compare this to a sonic log-derived value of the minimum horizontal stress S_h under the lateral constraint assumption that is often carried out in order to predict the "fracture gradient". For an isotropic rock mass

$$S_h = \frac{\nu}{1-\nu} S_V. \tag{A13}$$

and if the isotropic Poisson's ratio, as estimated from the sonic log V_P and V_S values, ranges from 0.2 to 0.25, S_h is estimated to be only 25%–33% of S_V. Applying the same conditions for a TI material where (Melendez Martinez and Schmitt 2015)

$$S_h = \frac{\nu_{13}}{1-\nu_{12}} S_V, \tag{A14}$$

will further reduce the estimated S_h magnitude. Such low values contradict those more directly obtained above.